

The following article has been submitted to Journal of Applied Physics. After it is published, it will be found at the following [Link](#).

Nature of point defects in monolayer MoS₂ and the MoS₂/(111)-Au heterojunction

Roozbeh Anvari¹ and Wennie Wang¹

McKetta Department of Chemical Engineering, University of Texas at Austin

Deposition of MoS₂ on (111)-Au alters the electronic properties of MoS₂. In this study, we investigate the free-standing MoS₂ monolayer and the MoS₂/(111)-Au heterostructure, with and without strain, as well as defects of interest in memristive and neuromorphic applications. We focus on so-called atomristor devices based on monolayer materials that achieve resistive switching characteristics with the adsorption and desorption of metal adatoms. Our study confirms that the formation of midgap states is the primary mechanism behind the resistive switching. Our results show that strain lowers the adsorption/desorption energies of Au+defect structures of interest, leading to more favorable switching energies, but simultaneously reduces the switching ratio between states of differing conductivities. The presence of the (111)-Au substrate additionally introduces non-uniform amounts of strain throughout and charge transfer to the MoS₂ monolayer. We propose that the induced strain can contribute to the experimentally observed *n*- to *p*-type transition and Ohmic to Schottky transition in the MoS₂ monolayer. The charge transfer leads to a permanent polarization at the interface, which can be tuned by strain. Our study has important implications on the role of the electrode as being a source of the observed variability in memristive devices and as serving as an additional degree of freedom for tuning the switching characteristics of the memristor device.

I. INTRODUCTION

Memristors are an emerging technology in low-power and highly integrated devices¹, data storage and encryption²⁻⁴, and neuromorphic computing circuits⁵. In memristors, the application of an external electric field modulates the electrical resistance between a high resistance state (HRS) and low resistance state (LRS) while retaining a memory of the prior resistive state¹. Non-volatile resistive switching (NVRS) has been observed across several 2D materials such as graphene oxide⁶, black phosphorous⁷, h-BN⁸, and various transition metal dichalcogenides (TMDs)⁹⁻¹². Atomically-thin monolayer materials exhibiting NVRS, dubbed atomristors¹², have been demonstrated to have switching voltages on the order of 1 V or less, making them suitable for low-power, energy-efficient devices¹¹. The use of (nearly) atomically-thin 2D monolayer materials additionally represents the ultimate material scaling limit for achieving high packing densities. Indeed, NVRS in monolayer materials has been observed to occur through the formation and dissolution of point defects, which avoids the stochastic formation of conductive filaments^{13,14} and may help realize energy-efficient devices with resistive switching^{11,12,15}. While point defects are broadly known to impact the electrical^{16,17}, optical^{18,19}, and magnetic properties^{20,21} of 2D materials, the mechanism(s) of how resistive switching arises from the presence of point defects is less well understood. We consider NVRS in vertically-stacked two-terminal devices consisting of a metal-semiconductor-metal. In particular, we focus on the interface between MoS₂ and gold, which is a commonly used contact metal due to its high electronic conductivity and chemical inertness.

Several theoretical and experimental studies have investigated the mechanism of resistive switching mediated by point

defects in MoS₂ on gold electrodes, but thus far a comprehensive picture is lacking. One proposed model from Hus et al.¹⁵ attributes the resistive switching behavior to the presence of metal adatoms adsorbed in existing sulfur vacancies and sulfur di-vacancies^{15,22}. By combining scanning tunneling spectroscopy and microscopy with DFT calculations, Hus et al. found such metal adatoms result in an in-gap state near the Fermi level that induces a greater degree of metallicity in the monolayer. This model was further refined in the work of Ge et al.^{11,12}, who proposed a mechanism in which the metal adatom dissociates from the electrode, may diffuse across the monolayer surface, and adsorbs onto an existing vacancy. Ge et al. suggested that a similar mechanism may broadly apply to 2D materials based on the observation of similar resistive switching characteristics in current-voltage measurements across several TMDs. These results were corroborated with first-principles calculations based on the Keldysh nonequilibrium Green's function theory from Li and colleagues²³ who considered point defects in free-standing MoS₂, as well as MoTe₂ and WTe₂. These studies focused mainly on the free-standing monolayer, neglecting the metal electrode(s). The theoretical work from Boschetto et al.^{24,25} computed tunneling probabilities of various concentrations of sulfur vacancies and adatoms in a heterostructure of MoS₂ and gold. Boschetto et al. proposed that the formation of metal adatom clusters forming a conducting bridge could induce a semiconducting to metallic transition in MoS₂. Nevertheless, several open questions remain: What, if any, is the role of the metal electrode in the resistive switching mechanism? More specifically, what is the role of the metal electrode in the defect energetics and the transport properties?

The interface between MoS₂ and gold metal contacts presents a wealth of physics that has been under-explored in the context of resistive switching. In building an atomic

understanding of the interface, one of the first considerations is the impact of strain. When an interface between monolayer MoS₂ and (111)-Au is formed, the Au substrate may lead to heterogeneous local strain throughout the MoS₂ monolayer. The extent to which the heterogeneity exists varies among studies and may vary depending on the method of preparation. For example, a study from Velický and colleagues reported biaxial strains of up to 1.9% based on the downward shift and broadening of the in-plane E' vibrational mode. In contrast, monolayer MoS₂ synthesized via chemical vapor deposition on polycrystalline Au has been reported to exhibit only out-of-plane strain and no in-plane strain²⁶.

Prior theoretical and experimental studies also suggest that variations at the MoS₂/Au(111) interface are intimately connected with the wide range of electronic properties reported²⁷⁻³¹. For example, McDonnell and co-workers²⁷ used a combination of XPS and STM/STS to correlate the observation of lower Schottky barriers to the presence of sulfur and molybdenum vacancies (i.e., varying stoichiometry in the monolayer). The surface roughness of the metal electrode, strain between the monolayer and substrate, and hence the interlayer spacing have also been invoked^{28,31,32} to explain the modulation of electronic properties between different metal electrodes or compared to free-standing MoS₂. However, only a few studies^{24,25,33} have considered the explicit presence of the metal electrode in the context of understanding resistive switching mechanisms. In these studies, the effects of strain, interlayer spacing, and the presence of defects are only partially considered or omitted. Hence, in this study, we seek to further elucidate the impact of the metal electrode and accompanying strain on the transport properties of monolayer MoS₂ and connect these insights to resistive switching as mediated by point defects.

The paper is organized as follows. We first discuss our computational methodologies for computing defect energetics, transport properties, and for constructing interfacial models between MoS₂ and (111)-Au in Section II. In Sections III A and III B, we discuss the formation of native point defects with gold adatoms in free-standing MoS₂ without strain and with strain. Our results confirm that the adsorption of a gold adatom induces large changes in conductivity to explain resistive switching in monolayer MoS₂. Next, we investigate the effects of biaxial tensile strain in the MoS₂/(111)-Au interface on the defect formation properties (Section III C), interfacial charge transfer and dipole formation (Section III D), Ohmic to Schottky transition and its effect on transport properties (Section III E). Finally, we conclude with a discussion of the implications of our calculations on resistive switching mechanisms.

II. COMPUTATIONAL DETAILS

First-principles electronic structure calculations based on density functional theory were conducted using the OpenMX

software package (version 3.9.2)³⁴⁻³⁶. Calculations were performed using norm-conserving pseudopotentials³⁷, the generalized gradient approximation for exchange correlation interactions³⁸, spin polarization, and pseudo-atomic localized basis functions. The standard basis set for the pseudo-atomic orbitals used for Mo was s3p2d2, for S was s2p2d1f1, and for Au was s3p2d2f1, all with cutoff radius of 7.0 a.u. A vacuum distance of 50 Å in the direction normal to the surface was used in the calculations. The atomic coordinates were relaxed until the interatomic forces were below 10⁻⁵ Hartree/Bohr. Brillouin zone sampling was performed using a 12 × 12 × 1 mesh, energy cutoff of 300 Ry and energy-convergence threshold of 10⁻¹⁰ Hartree. The DFT-D3 method is used in calculations involving the heterostructure to account for van der Waals interactions³⁹. Chemical potentials with respect to the vacuum level were evaluated via the effective screening medium (ESM) method⁴⁰, as implemented in OpenMX. In the projected density of states (PDOS) reported here, the Gaussian broadening width was set at 0.05 eV. Band unfolding procedures were performed with the LCAO method implemented in OpenMX⁴¹.

The formation energy of defects E^f provides information on the stability of a particular defect and is calculated using

$$E^f = E_{def} - E_{host} - \sum_i n_i \mu_i + q(E_v + E_F) + E_{corr}. \quad (1)$$

E_{def} and E_{host} correspond to the DFT total energies of the system with and without the defect, μ_i is the chemical potential of species i , and n_i represents the number of species i added ($n_i > 0$) or removed ($n_i < 0$). E_v and E_F are the valence band maximum (VBM) and Fermi level position, respectively. E_{corr} indicates the energy correction term corresponding to the spurious interactions between images of the defects within the periodic supercell approach and is included using the effective screening method⁴² as implemented in the openMX code. We consider only neutral defects in this paper ($q = 0$), namely the gold adatom adsorbed to sulfur vacancies, sulfur divacancies, and molybdenum vacancies as shown in Figure S1. The chemical potential of S is referenced to the solid, monoclinic phase; as such, $\mu_{Mo} = \mu_{MoS_2} - 2\mu_S$ and $\mu_{Au} = (\mu_{Au_2S} - \mu_S)/2$. The calculated heat of formation of monolayer MoS₂ is -0.988 eV/atom, which compares favorably to that on the Materials Project⁴³ (-0.964 eV/atom).

We consider the energetics of an Au adatom interacting with monolayer MoS₂. The adsorption energy is computed using $E_{ads} = E_{host+adatom} - E_{host} - E_{adatom}$, where E represents the computed DFT total energy and E_{adatom} is referenced to bulk gold. We also compute the binding energy of Au adatoms to existing native point defects (e.g., sulfur vacancies), which is computed as⁴⁴ $E^b = E_{vacancy+adatom}^f - E_{vacancy}^f - E_{adatom}^f$, where E^f represents a formation energy as defined in Eq. 1.

For transport calculations of free-standing MoS₂, the linearized semi-classical Boltzmann transport equation is solved

using the Boltztrap code⁴⁵ to compute the conductivity tensor

$$\sigma_{\alpha\beta}(T, \mu) = \frac{e^2}{V} \int \tau(i, \mathbf{k}) v_{\alpha}(i, \mathbf{k}) v_{\beta}(i, \mathbf{k}) \left[-\frac{\partial f_{\mu}(T, \varepsilon)}{\partial \varepsilon} \right] d\varepsilon, \quad (2)$$

where e , T , V , τ and f_{μ} are the electronic charge, temperature, the volume of the unit cell, the relaxation time, and the Fermi-Dirac distribution respectively. The band velocity of i th energy band $\varepsilon(i, \mathbf{k})$ is given by $v_{\alpha}(i, \mathbf{k}) = \frac{1}{\hbar} \frac{\partial \varepsilon(i, \mathbf{k})}{\partial k_{\alpha}}$ where k_{α} is the α component of the wavevector \mathbf{k} . The Brillouin zone was sampled with a k -point mesh of $32 \times 32 \times 1$. The electrical conductivity is obtained within the constant relaxation time approximation (CRTA). The CRTA is based on the assumption that the relaxation time does not change significantly with energy within the relevant range of the Fermi level and is thus taken to be approximately a constant ($\tau(i, \mathbf{k}) \approx \tau$). In this study, we compute a normalized conductivity ($\bar{\sigma} = \sigma/\tau$). This approximation scheme is computationally efficient and has been widely applied to study TMDs and other 2D materials^{46,47}. However, its predictive power of the absolute conductivity depends on the empirical choice of scattering rate^{48–50}. We emphasize that this study on resistive switching is focused on the ratios of the conductivity between the low- and high-resistance states. As such, we expect ratios involving $\bar{\sigma}$ to be weakly dependent on the details of the relaxation time τ . Thus, trends in the transport properties of the defects investigated here are expected to be retained.

We next describe our rationale for constructing various heterostructures of monolayer MoS₂ on (111)-Au. We focus on the MoS₂/(111)-Au heterostructure and find this structural model captures many features of the Au/MoS₂/Au vertical stack, as detailed in the Supplementary Information (Figure S2). Our calculations indicate that the formation energy of sulfur vacancies are converged to within 1.3 meV for a (6x6) supercell with a vacuum of 55 Å, which corresponds to a defect density of $3.14 \times 10^{13} \text{ cm}^{-2}$. Details of convergence are given in the SI. MoS₂ is known to go through a ($\sqrt{3} \times \sqrt{3}$) reconstruction when deposited on (111)-Au^{51–53}. Our calculations yield a lattice mismatch of 5.79% between relaxed lattice constant of the top reconstructed layer ($2\sqrt{3} \times 2\sqrt{3}$) – MoS₂ (11.06 Å) and that of the (111)-Au substrate (11.75 Å). Previous experimental studies indicate that different levels of biaxial strain are present in the MoS₂ top layer after deposition on (111)-Au^{28,31,32}. Thus, we study the effect of strain in two extreme scenarios in which MoS₂ goes through a biaxial tensile strain to adapt to the lattice vectors of Au and vice versa (i.e., 0% to 6.23% strain of MoS₂); four additional intermediate structures are chosen in which both MoS₂ and (111)-Au are strained, as depicted in Figure S11a.

III. RESULTS

A. Point defects in free-standing monolayer MoS₂

It has been suggested that the adsorption of gold on monolayer MoS₂ is responsible for the resistive switching^{15,23}. In order to understand the influence of point defects, we consider the sulfur vacancy (V_S), sulfur divacancy (V_{2S}), molybdenum vacancy (V_{Mo}); this is in addition to the defect relevant to resistive switching, i.e., a gold adatom adsorbed on the pristine monolayer Au + pr and on each of the vacancies considered (Au_S, Au_{2S}, Au_{Mo}). To begin, we report on the defect formation energies of the vacancies without an Au adatom (see also Figure S3 and Table S1 in the Supplementary Information). The molybdenum vacancy V_{Mo} is predicted to be the least stable vacancy with a formation energy of at least 4 eV (in sulfur-rich conditions). The sulfur divacancy V_{2S} is the second most stable defect over a wide range of the chemical potentials of sulfur, and only becomes less favorable than the molybdenum vacancy (V_{Mo}) in extremely sulfur-rich environments. Our calculations confirm that the single sulfur vacancy (V_S) is the most energetically favorable vacancy for all ranges of chemical potential of S, in agreement with prior computational studies⁵⁴. Our observations of the relative stability of vacancies in MoS₂ are also in line with experimental observations based on STM/STS¹⁵.

We next consider the incorporation of an Au adatom on a sulfur vacancy site Au_S, a sulfur divacancy site Au_{2S}, and a molybdenum vacancy site Au_{Mo} (corresponding structures in Figure S1). The defect formation energy phase diagram of the cation and anion vacancies of MoS₂ containing an Au adatom is depicted in Figure 1a. Figure 1a shows that the formation energy of an Au-adatom adsorbed onto the pristine structure at the Mo, the S, or the hollow sites are within several meV of each other and comparable to the defect formation energy of the sulfur vacancy under sulfur-rich conditions. We find that the formation energy for the direct substitution of Au for a sulfur site across relevant ranges of the sulfur chemical potential is unfavorable ($\sim 1.6 \text{ eV}$ to 3.5 eV) compared to the adsorption energy of Au onto a pre-existing sulfur vacancy (0.95 eV). These results indicate that the adsorption of an Au adatom onto a pre-existing anion vacancy is a primary mechanism for resistive switching in atomristor devices, in alignment with prior studies^{15,23,55}.

In addition to the stability of the defect complexes considered, we consider the impact of the various defect complexes involving an Au adatom and vacancy on the electronic structure and the change in conductivity. The electronic structure (unfolded band structure and DOS) and normalized electrical conductivity of MoS₂ structures with a vacancy and Au+vacancy defect complex are depicted in Figures 1 and S4. Analysis of the band structure indicates that all the vacancy defects and their complexes with Au have a direct band gap at the high-symmetry K-point. Both V_S and V_{2S} defects induce midgap states, approximately 0.5 eV below the conduction band minimum (CBM), while V_{Mo} induces several mid-gap states that are located farther from the CBM.

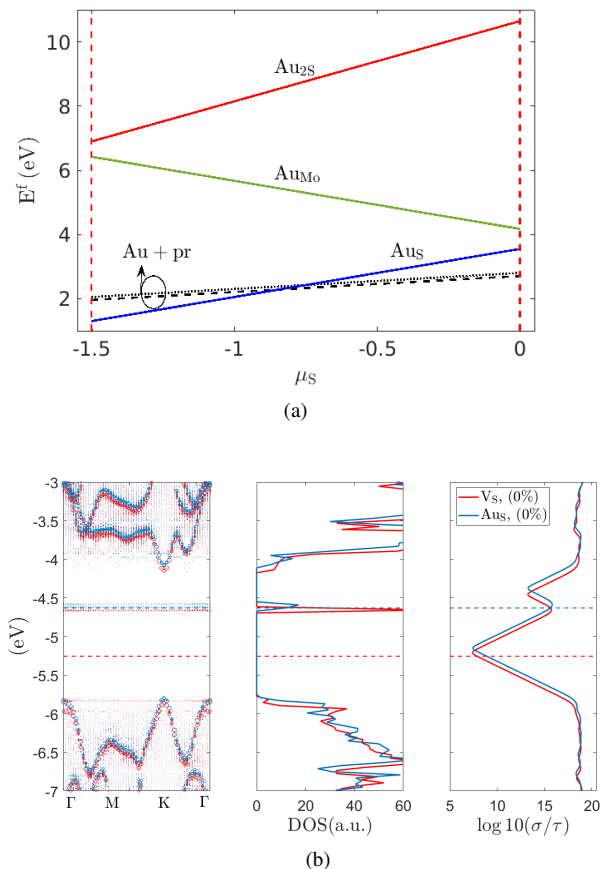


FIG. 1. (a) Calculated formation energies of a number of defect complexes involving an Au adatom and native vacancy in standalone MoS_2 . (b) Unfolded bandstructure (left), DOS (middle) and normalized electrical conductivity (right) of (6×6) supercell of MoS_2 with Au adatom adsorbed on various cation and anion vacancies. The electronic structure and corresponding normalized conductivity of the sulfur divacancy and molybdenum vacancy with and without an Au adatom are provided in Figure S4.

From our analysis of the unfolded band structure, we find minimal changes of the electron velocity near the band edges (K-point). As a result, the difference in normalized electrical conductivity is determined by the density of states (see Eq. 2).

Based on a density of states argument, one would expect a high (normalized) conductivity when the Fermi level is resonant with a partially filled electronic state, either of the defect or of the host monolayer. We focus here on Au_S and present the same data in Figure S4 for the remaining defect configurations. As observed in Figure S4a, the pristine monolayer indeed has a negligible electrical conductivity in the vicinity of the computed Fermi level, which lies within the bandgap. When introducing a sulfur vacancy (Figure 1b), unoccupied defects emerge and are energetically separated from the computed Fermi level, leading to a moderate (4–5 orders of magnitude) increase in the normalized conductivity. By contrast, the introduction of a molybdenum vacancy (Figure S4) leads to defect states resonant with the com-

puted Fermi level, resulting in the normalized conductivity increasing by nearly ten orders of magnitude compared to the pristine monolayer case. As such, the adsorption of Au on the molybdenum vacancy site leads to a minimal change in the computed normalized site conductivity. However, the formation energy of molybdenum vacancies is high and thus would not be expected to contribute significantly to the resistive switching of the overall device. Notably, the Fermi level of configurations involving the gold adatom (e.g., Au_S and $\text{Au} + \text{pr}$ structures) are located at the energy level resonant with the energy of the midgap defect state. Thus, based on the formation energy and transport properties of these defects, one would expect the resistive switching to be mediated predominantly by the presence of sulfur vacancies with some but limited contribution from divacancies, in line with experimental observations¹⁵. Indeed, the normalized conductivity increases by several orders of magnitude when considering the adsorption of an Au adatom onto the sulfur vacancy (around ten orders of magnitude) and divacancy sites (around five orders of magnitude). Previous experimental work shows that the ON/OFF ratio, or the ratio of resistance at LRS to that of HRS, can reach 10^8 ^{12,53}. Calculated normalized conductivities corresponding to native defects complexes are tabulated in Table S2.

Thus far, we have a basic understanding of a resistive switching mechanism in atomrystals to be mediated by the formation of point defect complexes involving the adsorption of Au adatoms. We investigate next the effect of strain and the presence of the metal electrode/substrate, separately (Section III B) and in conjunction (Sections III C and III D).

B. Effect of strain in free-standing monolayer MoS_2

In this section, we explore the effect of biaxial tensile strain on free-standing MoS_2 . The changes of the band edges of the pristine MoS_2 structure with biaxial tensile strain are depicted in Figures S6, S7, and S8. At zero strain, the band gap is direct with dominant character from the out-of-plane Mo (d_{z^2}) states at the CBM located at the high-symmetry K-point; the VB edge at the K contains contributions from the in-plane ($d_{x^2-y^2}$) and the VB edge at Γ contains contributions from out-of-plane (d_{z^2}) orbitals of Mo. As the tensile strain increases (0 to 5%), the states with Mo: d_{z^2} and S: p_z character shift up relative to E_f by approximately 0.54 eV and the VBM mainly consists of Mo: d_{z^2} at higher tensile strain (Figure S8). As a result, the band gap energy of the strained structure shrinks and becomes indirect. Moreover, the band velocity increases at both CBM (K-point) and VBM (Γ -point). Therefore, it is expected that changes of group velocity play a pronounced role in the conductivity of strained structures (either with or without defects).

With this in mind, we consider the effect of biaxial tensile strain on the electronic structure and conductivity of free-standing monolayer containing defects. We consider the pristine monolayer, the monolayer with a sulfur vacancy and

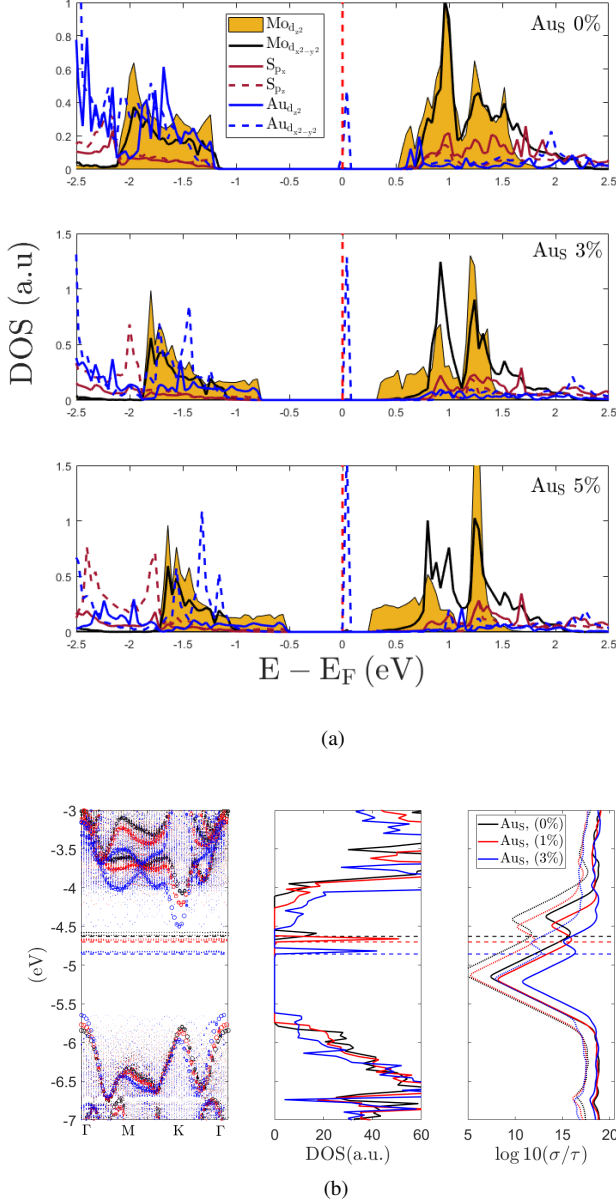


FIG. 2. (a) Effect of biaxial tensile strain of the projected density of states. (b) Effect of biaxial tensile strain on the electronic structure, in-plane conductivity (thick solid lines), and out-of-plane conductivity (dotted thin lines) of defective MoS₂ containing an Au adatom adsorbed on a sulfur vacancy.

pristine monolayer with Au adatom as relevant defects to resistive switching; in particular, we focus on the Au adatom adsorbed on a sulfur vacancy in Figure 2. Figure S6 shows the corresponding results for the pristine monolayer, MoS₂ with a sulfur vacancy only, and pristine MoS₂ with an Au adatom adsorbed.

When including the effect of strain with the adsorption of an Au adatom on the pristine surface, we again observe similar changes in the band edges of free-standing monolayer

MoS₂. The inclusion of an Au adatom on the pristine monolayer introduces a defect level that is 759 meV below the CBM, which is resonant with the Fermi level. As the strain increases from 0 to 5%, the defect level gets closer to the CBM but remains resonant with the Fermi level. Notably, the midgap defect state consists of mainly of Au:*d*_{z2} character followed by Mo:*d*_{z2} character. As tensile strain increases, the contribution of Au:*d*_{z2} character to the defect level increases and arises from the relaxation of the Au adatom minimizing its distance to the plane of the monolayer, leading to a greater interaction between the Au adatom and monolayer (see Tables S4 and S5 for changes in measured distance and occupations with strain).

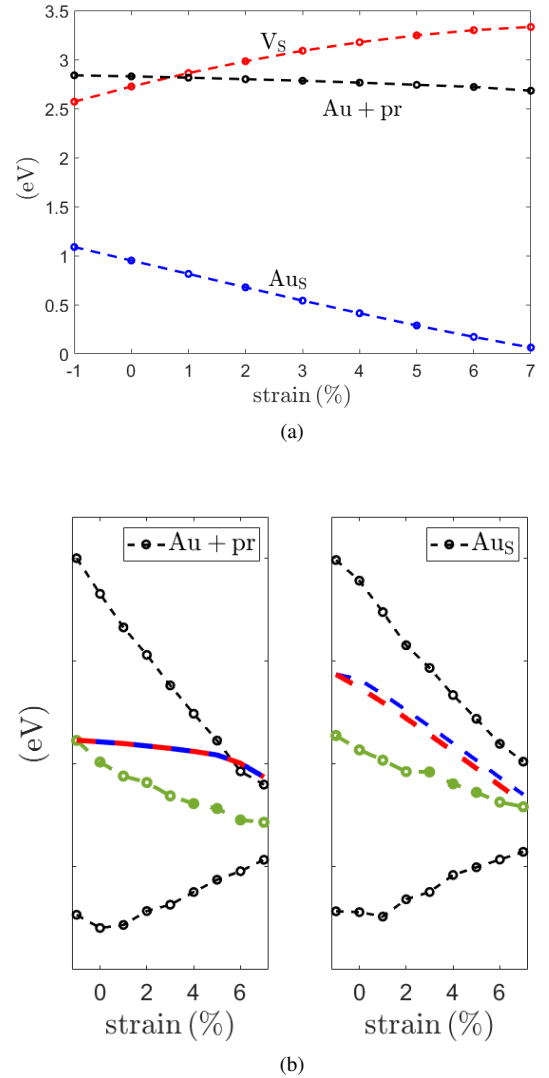


FIG. 3. (a) Effect of strain on formation energy of V_S and adsorption energy of the Au adatom on the pristine structure Au + pr and sulfur vacancy Aus. (b) Effect of strain on the band edges of Aus and Au + pr structures. Dashed blue lines correspond to defect level and red lines correspond to the Fermi-level. Center of the d-band is shown by green. Effect of strain on the band edges of pristine and V_S are given in S9.

We also present in Figure 2 the results for an Au adatom adsorbed on a sulfur vacancy in free-standing MoS₂. The midgap defect state in Au_S is resonant with the Fermi level. Unlike the defect level in the Au+pr configuration, the defect level in the Au_S configuration interestingly consists mainly of Au: $d_{x^2-y^2}$, illustrating the different degree of hybridization of the Au adatom with the monolayer when sulfur vacancies are present. An analysis of the orbital decomposition of the unfolded bands in Figure S7b indicates that strain leads to the following changes in the electronic structure for MoS₂ containing an Au adatom at a sulfur vacancy.

Figure 3a shows that the adsorption energy of the Au adatom on the pristine and defective structures decreases with increasing tensile strain. We can rationalize this trend based on the d -band center theory^{56,57}. Here, the d -band center is considered to be the average of the lowest energy level of the unoccupied and highest energy level of the occupied Mo d_{z^2} bands. Tensile strain leads to a reduction of the wavefunction overlap in the vicinity of the adsorption site and consequently a narrowing of the d -bands. In the case of an early transition metal such as Mo, the narrowing of the d -bands leads to a decreased population of the d -bands. Due to charge conservation, the d -bands will shift downward, leading to a higher occupation of the anti-bonding orbitals. This downward shift of the d -bands corresponds to a weakened interaction between the adsorbate and the surface. Figure 3 shows the computed d -band center with respect to the band edges and Fermi level as a function of tensile strain, in agreement with the trend in computed adsorption energies.

Accompanying these shifts in the d -band is a redistribution of charge in the vicinity of the defect site, as shown in Figure 4. We observe that the vicinity of the Au_S defect experiences a net loss of charge with increasing tensile strain whereas the vicinity of Au + pr undergoes a net gain of charge with increasing tensile strain. From Figures 3 and S7, we observe that the center of d_{z^2} band gets closer toward the Fermi level with increasing strain, while that of $d_{x^2-y^2}$ shifts away from the Fermi level in all defect configurations considered. Therefore, it is expected that the d_{z^2} orbital becomes more populated while the $d_{x^2-y^2}$ orbital becomes less populated as the tensile strain increases. Indeed, as shown in Tables S4 and S5, the orbital-decomposed charges of Au + pr and Au_S structures confirms this trend. We revisit these trends when considering the heterostructure of Mo₂ and gold.

We briefly comment on the apparent Fermi level pinning of the Au + pr defect configurations. Several experimental studies have reported that Fermi level pinning occurs for MoS₂ in contact with metals^{31,53}. The mechanism of the observed Fermi level pinning at the MoS₂/Au(111) interface has been attributed to formation of interfacial dipoles (as discussed in section III D and III E). Notably, this mechanism is distinct from well-known Fermi level pinning mechanisms that are applicable to common metal-semiconductor junctions⁵³: (1) Bardeen^{58,59}, (2) metal induced gap states^{60,61}, (3) defect

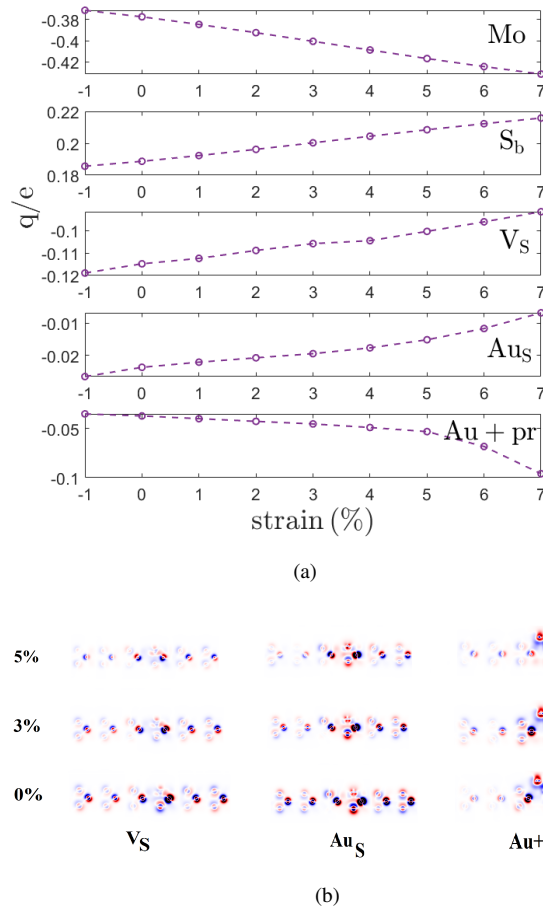


FIG. 4. (a) Effect of biaxial strain on the Mulliken charge on Mo and S of pristine structure (demonstrating an overall charge delocalization), S-vacancy of the V_S structure, and Au-adatom adsorbed on Au_S and Au + pr structures. Accumulation and depletion of charge is represented by positive and negative signs, respectively. (b) 2D-cross section of the charge-difference positive and negative numbers, respectively. The charge difference is obtained by $\rho_{\text{defect}} - \rho_{\text{pr}} \mp \rho_{\text{adsorbate}}$ (positive for vacancy and negative for adsorbate). Here red and blue colors correspond to loss and gain of charge density, respectively.

induced gap-states⁶². Interestingly, the Fermi level in the Au_S defect configuration is resonant with the defect level introduced by the Au adatom at all strain levels considered. Furthermore, our calculations (see Figure 3) show that strain in free-standing monolayer Mo₂ can induce an n -type to more p -type-like transition for defective structures, as reported in previous theoretical reports^{50,63}. In section III E we connect this discussion of the changes in electronic structure with strain and defects to understand experimental observations of n - to p -type-like transition in MoS₂/Au(111) structures^{27,28}.

Finally, we consider the effect of strain on the normalized conductivity. Figure 5 shows the effect of biaxial strain on the normalized tensor elements of electrical conductivity of the free-standing pristine and defective structures. In all cases

considered (i.e., the pristine structure, Au + pr, V_s , Au_s), tensile strain leads to an increase in the normalized conductivity. As shown in Figure 2, the increase of the magnitude of the normalized conductivity in strained structures is due to the increase of the band velocity, which is apparent in the band edges for both the in-plane and out-of-plane conductivities. As shown in Figure 2b, the normalized conductivity reaches a local maximum when the Fermi level is resonant with the energy level of defect. Thus, the normalized conductivity of defects with an Au adatom are generally higher than those without an Au adatom due to the Fermi level being resonant with the corresponding defect level in the former case. As the monolayer is strained, we also observe the computed Fermi level follow the downward shift of the defect level. We find a similar trend for the pristine monolayer, the monolayer containing a sulfur vacancy, and the pristine monolayer containing an Au adatom (Figure S6).

In the context of resistive switching, it is the ratio of conductivity between the high-resistance and low-resistance states that is relevant. Figure 5b provides the ratio of the normalized conductivity at ON/OFF states for in-plane (xx) and out-of-plane (zz) components. We focus on the ratio between involving the resistive switching event between the sulfur vacancy alone and the Au adatom adsorbed on the sulfur vacancy ($\sigma_{Au_s}/\sigma_{V_s}$). For $\sigma_{Au_s}/\sigma_{V_s}$ the ratio of the normalized conductivity across the monolayer diminishes by around five orders of magnitude going from 0% to 2% strain in the MoS_2 monolayer. For reference, the switching ratios reported in the literature are in the range of 6-8 orders of magnitude¹⁵ (red line in Figure 5). While some degree of resistive switching via point defects is preserved up to large strains, we anticipate that the consideration of strain in resistive switching devices based on 2D materials can explain some of variability observed within and among samples and will be an important factor in comparing the performance (in this case, the switching ratio) among materials platforms and sample preparation methods.

C. Point defects and strain in the $MoS_2/(111)$ -Au heterostructure

We now discuss the influence of the metal substrate using the $MoS_2/(111)$ -Au heterostructure. The presence of the metal substrate is analyzed from the perspective of introducing strain into the monolayer and in driving charge transfer to the monolayer. As with the discussion of the free-standing monolayer, we consider the impact of each of these effects in the presence of defects relevant to memristor devices. With the formation of a heterostructure, we distinguish between the sulfur in the vicinity of the defect that is closest to the substrate S_b and farthest from the substrate S_t . Figure 6a depicts that the presence of the substrate leads to an increase of the formation energy of the sulfur vacancy and divacancy (we omit the Mo vacancy as it has already a high defect formation energy without the substrate). In contrast, the

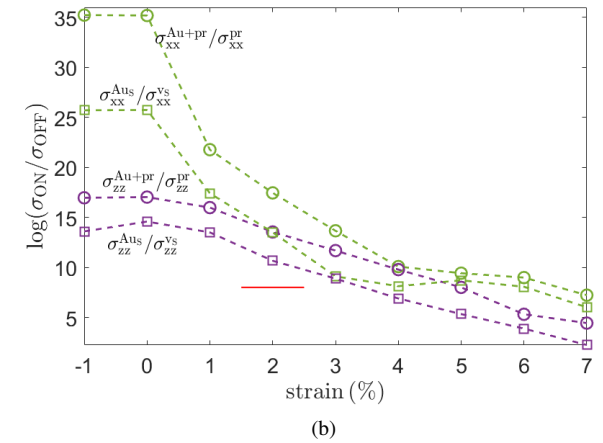
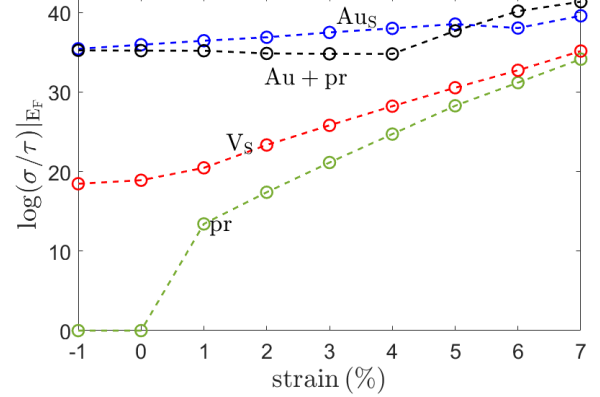


FIG. 5. (a) Effect of biaxial strain on the normalized electrical conductivity of stand alone pristine MoS_2 structure (green), V_s (red), Au_s (blue) and Au + pr (black) structures at Fermi-level at 300 K in units of $1/\Omega \cdot cm \cdot s$. (b) Calculated switching ratio of Au_s/V_s (squares) and Au + pr/pr (circles) combinations of transport in the lateral (dashed) and perpendicular direction (solid) based on normalized conductivities. The red line corresponds to experimental value of the switching ratio⁵³.

presence of a gold substrate leads to a decrease of adsorption energies compared to the free-standing monolayer (calculated energies are tabulated in Table S8 of SI), including with tensile strain included. As a result, we conclude that the adsorption of an Au adatom on a pre-existing vacancy is the dominant defect responsible for switching, rather than direct substitution of a Au adatom for sulfur, consistent with the conclusions of the free-standing monolayer.

Next, we examine the electronic structure of the $MoS_2/Au(111)$ heterostructure under strain to understand the trends observed in the computed ON/OFF ratio. The PDOS of defect complexes in the $MoS_2/Au(111)$ heterostructure under 0, 1.24 and 6.23% biaxial strain is depicted in Figure 6b (see also Figures S15, S16 and S17). For the heterostructure with 1.24% strain, a typical strain found in experimental samples, the band gap decrease to 1.32 eV and the Mo: d_{z^2} orbitals

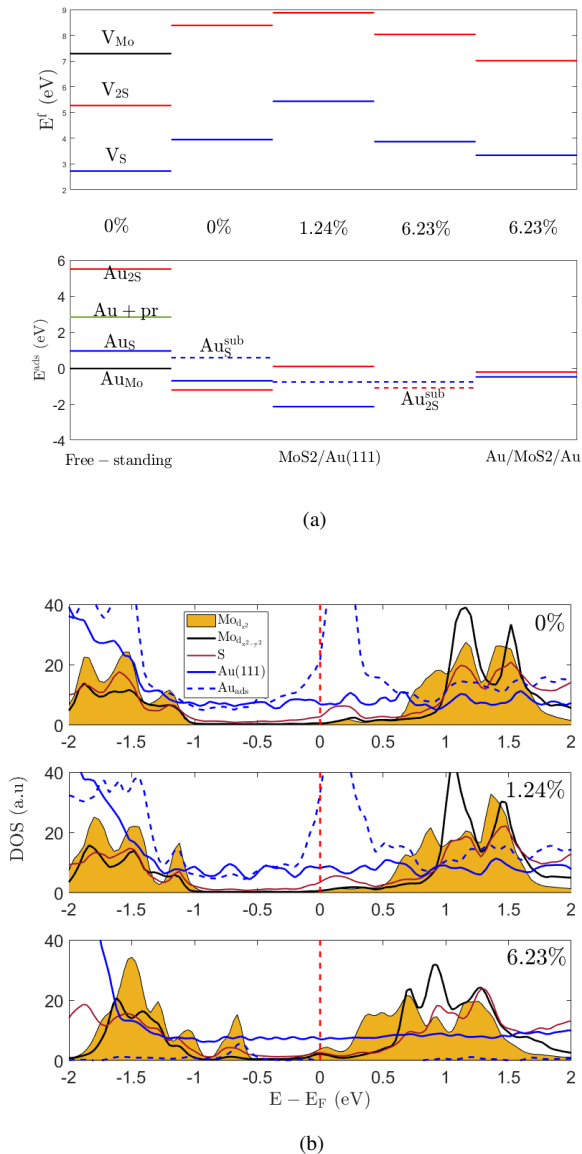


FIG. 6. (a) Effect of tensile strain on the formation energy of vacancies (top) and adsorption energy of Au+vacancy structures. Columns from left to right correspond to Free-standing MoS₂, MoS₂/Au(111) heterostructure under 0%, 1.24% and 6.23% tensile strain, and double electrode structure under 6.23% tensile strain, respectively. Adsorption energies represented by solid (dashed) line correspond to Au-adatom provided by an external reservoir (substrate). Calculated energies are tabulated in Table S8 of SI. (b) Electronic structure (DOS) of Au_S+V_S defect complex in the MoS₂/(111) – Au heterostructure. A more complete picture is given in Figures S15, S16, and S17.

have shifted towards the VBM, as also observed in the free-standing monolayer. Adsorption of Au into the vacancy (Au_S) still leads to a defect energy level, which is within 0.16 eV of the Fermi level. This behavior is also observed for the Au_{S2} defect configuration. The Au_{2S} structure sees two additional peaks located at 0.04 and 0.68 eV relative to the Fermi level. A comparison between the studied strained structures

indicates that at very high strain (6.23%) the electronic states at the band edges and Fermi level are then dominated by Mo: d_{z^2} orbitals. Consequently, high levels of strain lead to a suppression of the defect state induced by the adsorption of a Au adatom. Therefore, although high levels of strain significantly lower the adsorption/desorption energy levels, we expect that strain concurrently leads to a suppression of the expected switching ratio, as similarly found for the stand-alone monolayer. While beyond the scope of this paper, a rigorous study of the transport properties across the vertical stack architecture would quantify the impact of the presence of the MoS₂/(111)-Au interface and is a topic of future study.

D. Strain and charge transfer in the Mo₂/(111)-Au heterostructure

In this section we discuss how charge transfer across the heterostructure varies with increasing tensile strain and leads to different interfacial dipole moments. Figure 7 shows that increasing biaxial tensile strain leads to a reduction of the interlayer spacing between MoS₂ and the gold substrate (see also Figure S11a). Accompanying the change in interlayer spacing with strain are changes in the charge transfer between MoS₂ and gold electrode. Charge difference plots (S11b) show that more charge is accumulated on both the S_b atom and the surface of the electrode with increasing strain and decreasing interlayer spacing. As a result, a space charge region forms in the interfacial area and forms permanent dipole moments. Moreover, the surface integral of the charge depletion region, corresponding to $\Delta\rho < 0$ regions in Figure 7b, is larger at the boundary of the interfacial region near the electrode at low strain regimes and near MoS₂ at high strain regimes. This results in a permanent interfacial dipole moments to be pointing toward the electrode at low strains and pointing toward MoS₂ at high strains. Although the magnitude of the charge accumulation at both sides of the heterostructure is larger for higher levels of strain (corresponding to darker colors in Figure S11b), the decrease of the interlayer distance lowers the magnitude of the dipole moment. These phenomena are expected to contribute to the observed the n - to p -type transition and Ohmic to Schottky transition in experimental results, as discussed in the next section. We also expect this dipole to affect the dynamics of the resistive switching and to be an additional degree of freedom with which to modulate the resistive switching characteristics, a topic we leave to future study.

E. Strain and defects in the heterostructure and the Ohmic to Schottky transition

In this section, we present the relationships among strain, the interlayer spacing, and changes of the Schottky barrier height ϕ at the interface. This correspondence is first illustrated with the heavily strained (6.23%) and initially

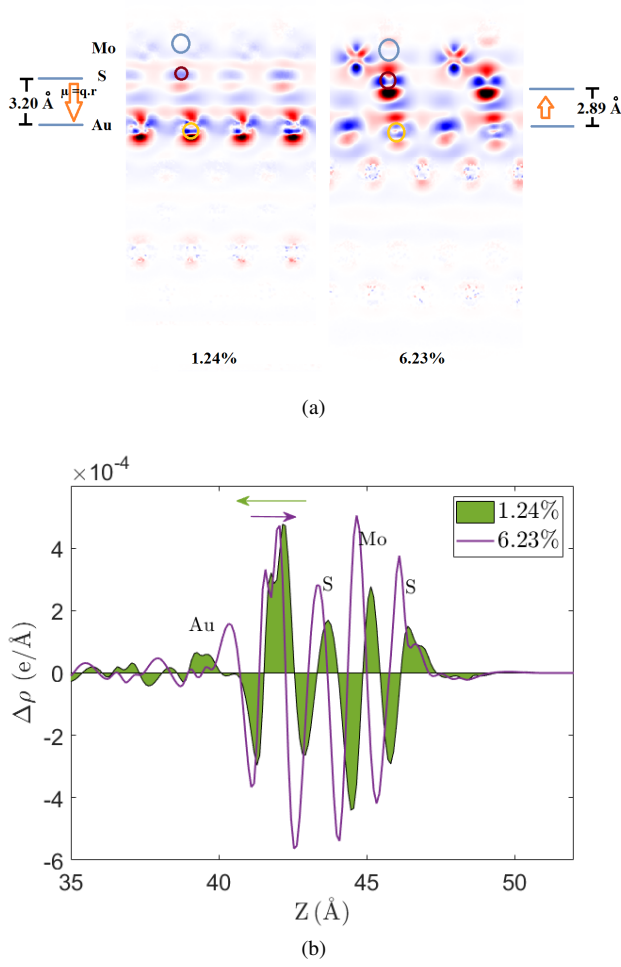


FIG. 7. (a) Charge difference plot and interlayer distances due to biaxial strain caused by lattice mismatch of the top MoS₂ layer with the (111)-Au substrate. The charge difference is obtained by $\rho_{\text{heterostructure}} - \rho_{\text{Au(111)}} - \rho_{\text{MoS}_2}$. Gold, red and blue circles correspond to the location of the surface of (111)-Au, S and Mo atoms, respectively. The blue bars and the arrow in between represent the interlayer distance and the magnitude and direction of the interfacial dipole moment, respectively. Lattice constants, interlayer distances and the corresponding charge difference plot of the other strained heterostructures are given in S11. (b) Cross section of the charge difference density along the direction normal to the surface.

Ohmic heterostructure in Figure 8a, which shows the changes in the average electrostatic potential along the direction normal to the surface with variable interlayer distance. Our results indicate that an increase of 0.55 Å in the interlayer distance brings the heavily strained and initially Ohmic heterostructure (6.23%) to the verge of transitioning to a Schottky interface; a further increase of the interlayer distance results in additional elevation of the barrier height above the Fermi level into the Schottky regime. Contrary to case of free-standing Au_s and Au + pr, where the adsorbed Au-adatom donates charge to the host MoS₂, the adsorbed Au-adatom formed in the Au_s/(111)-Au structure obtains extra electronic charge. As shown in Figure S18, the relative

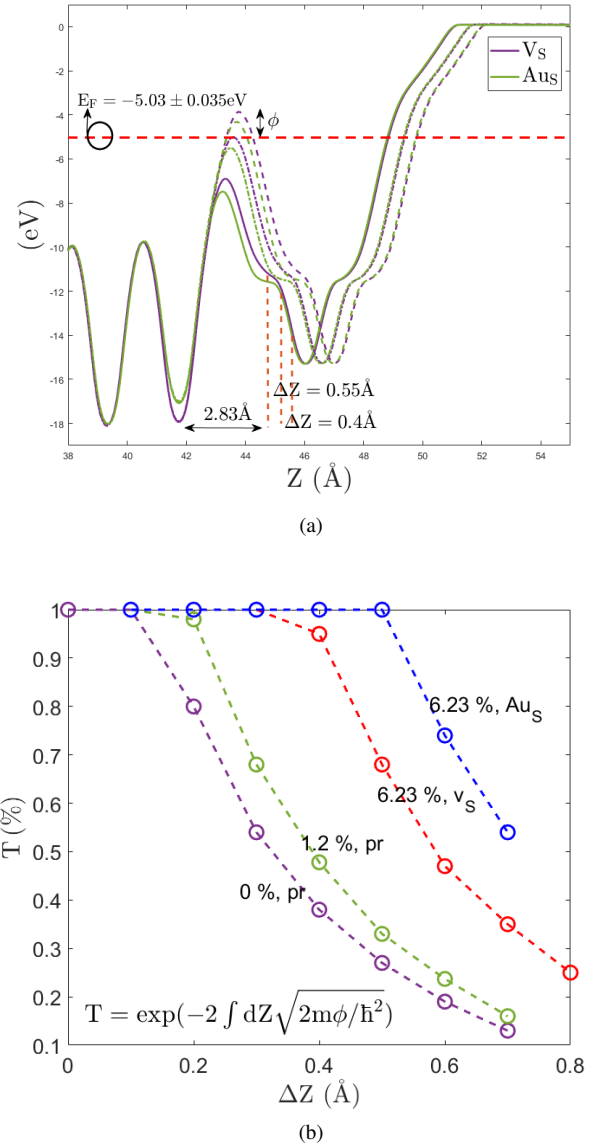


FIG. 8. (a) Changes of the electrostatic potential of atoms with interlayer distance of the MoS₂/(111)Au heterostructure under 6.23 % tensile strain. (b) Changes of tunneling probability with interlayer distance for select MoS₂/(111)-Au heterostructures. Changes of the corresponding Mulliken charges are given in Figure S18.

changes of the Mulliken charges of the Au(111) electrode and S_b also show an extremum at $\Delta Z=0.5$ Å, which is the onset of Schottky to Ohmic transition and is an indicator of the change of the direction of the interfacial dipole moment.

We repeat the calculation of the average electrostatic potential at different representative strains for a number of interlayer spacings and select defect configurations. Figure 8b demonstrates the effect of strain on the tunneling probability T and the corresponding interlayer spacing at which the Ohmic to Schottky transition occurs. Biaxial tensile strain lowers the barrier height, which is equivalent to an increase

in the onset (i.e., required shift of the interlayer distance) of the Ohmic to Schottky transition. Moreover, diffusion of the Au-adatom from electrode into a sulfur vacancy in the MoS₂ layer lowers the barrier and increases the tunneling probability. Therefore, the change of barrier height is an additional degree of freedom that contributes to switching mechanism, as influenced by strain, interlayer distance, and defects. This parameter is clearly a function of biaxial tensile strain caused by the deformation potential; we further suggest that the variation of the interlayer spacing is a descriptor of the varying surface roughness of the underlying Au(111) electrode. These results suggest that variability in the metal electrodes is transferred to the electronic and transport properties of the monolayer.

There are several implications to memristor devices that our results have. There is a plethora of theoretical and experimental evidence that hint at such variations in the deformation potential of MoS₂/(111)-Au interface. For example, experimental results have reported seemingly random n -type and p -type behavior with Fermi level fluctuations up to 1 eV^{27,28}. Moreover, a Schottky to Ohmic transition has been observed for samples grown under the same conditions^{28,29}. Ballistic electron emission microscopy experiments, which studied the growth of Au on Mo₂, also reveal that the roughness and deformation of Au grown on MoS₂ increases thickness of the Au layer^{28,29}. Raman spectra also reveal the emergence of tensile strain in the MoS₂ with thicker Au films. Here, with increasing thickness of Au, the interlayer distance and Schottky barrier increase whereas the transmission exponentially decreases through the (111)-Au/MoS₂ junction, though controversy of the exact nature of the transition remains²⁹. Interestingly, experimental studies report that the strength of interaction between monolayer MoS₂ and gold can be tuned when varying the surface roughness of the gold substrate^{64,65}.

Thus, our results show that the barrier height is affected by the deformation potential of the electrode and the resulting interfacial dipole moments. As an example of the importance of this concept in memristors, Hus et al.¹⁵ observed in scanning tunneling spectroscopy studies both an Ohmic-like and Schottky-like behavior in the I-V characteristics of sulfur vacancies in different locations on monolayer MoS₂. Their experiment suggest that the local environment of sulfur vacancies may differ and further impact the transport properties when a metal adatom is introduced. Our results suggest that the Ohmic and Schottky behavior correspond to either regions with high and low strain levels, or regions with different interlayer spacings due to surface morphology of the electrode.

IV. CONCLUSION AND FUTURE WORK

In this study, we explored the role of strain and the presence of the substrate for point defect complexes relevant to resistive switching applications for free-standing MoS₂ and

the (111)Au-MoS₂ junction. Specifically, we inspected the characteristics of neutral sulfur vacancies, sulfur divacancies, and molybdenum vacancies of MoS₂ and their interaction with an Au adatom in biaxially strained configurations of the free-standing monolayer and the interface with (111)-Au.

For the free-standing monolayer, our results indicated that formation of Au₅ structure is not energetically as favorable as that of Au + pr structure, suggesting that Au adatoms adsorb onto a pre-existing anion vacancy and that Au + pr structure serves as an intermediate state. Our calculations also showed that mechanical strain lowers the adsorption energy of the Au adatom, making the resistive switching energetically more favorable. The lowering of the adsorption energy may be rationalized using the d -band center theory from electrocatalysis. The change in the normalized conductivity (σ/τ) is found to arise from the Fermi level being resonant with the defect level induced by the Au adatom; changes of band velocities with tensile strain is a secondary effect of strain in free-standing structures. However, increasing tensile strain is found to lower the switching ratios of the ON/OFF states for all of the defect configurations considered. Consequently, any use of strain engineering in the 2D monolayer must balance the advantages of lowering the adsorption/desorption energies, i.e., switching energies, and the disadvantages of reducing the ON/OFF switching ratio in the design of memristor devices.

For the heterostructure of MoS₂/(111)-Au, we consider the effects of strain and charge transfer across the interface. The lattice mismatch between the substrate and MoS₂ causes tensile strain in MoS₂. Our study showed that the formation energies of all vacancies in the heterostructure increase and adsorption/desorption energies of Au+defect complexes of interest decrease with increasing tensile strain. Thus, the formation of an Au-adatom on a pre-existing vacancy is still more favorable, as it is in the free-standing monolayer. We find that moderate levels of strain (1.9%) bring the defect level of adsorbed Au-adatom closer to the Fermi level, suggesting a slight improvement in switching ratio. In contrast, very high levels of strain lead to a suppression of the electronic states from Au-adatom in the band-gap region, resulting in a diminished change in conductivity in the ON state, which is not favorable for resistive switching.

A second effect due to the presence of the electrode is the interfacial charge transfer and formation of interfacial dipole moments. Our calculations show that the magnitude and direction of the interfacial dipole moments change with tensile strain and interlayer distance between the electrode and monolayer. Thus, we suggest that a primary mechanism behind the experimental observation of n - to p -type behavior and the Ohmic to Schottky transition is related to the deformation potential of the Au(111) electrode. Indeed, our results suggest that the variability in performance often observed within and across memristor devices can be explained through this picture of strain, charge transfer, and interlayer spacing. This phenomenon can be affected and potentially

controlled through engineering processing conditions, chemical doping, strain, and electric field. Simultaneously, the presence of the electrode introduces additional degrees of freedom (e.g., the dipole moment) that can be used to alter the resistive switching response of the device. We leave this and the study of electric field and transport of the heterostructure (i.e., device) to future work.

In summary, we find that there are quantitative impacts that the presence of strain and the substrate have on the defect energetics related to the switching energy and transport properties related to the switching ratio of the atomristor. Therefore, the interaction of the monolayer and electrode is an important consideration in the search of the ideal atomristor.

V. SUPPLEMENTARY MATERIAL

The following supplementary information is provided: (1) Section S1: structural models of defect configurations and heterostructure, defect energetics, details electronic structure and transport properties of remaining defect configurations; (2) Section S2: effect of biaxial tensile strain in free-standing MoS₂ on the electronic structure, transport properties, orbital occupations, and charge density; (3) Section S3: effect of biaxial tensile strain in the MoS₂/(111)-Au heterostructure on charge density, site occupations, defect energetics, and electronic structure.

ACKNOWLEDGMENTS

We thank Deji Akinwande for valuable discussions. The work was supported in part by The Welch Foundation (grant F-2172-20230405). The authors acknowledge the Texas Advanced Computing Center (TACC) at The University of Texas at Austin for providing HPC resources that have contributed to the research results reported within this paper. URL: <http://www.tacc.utexas.edu>

VI. REFERENCES

- ¹T. Chang, S.-H. Jo, and W. Lu, "Short-term memory to long-term memory transition in a nanoscale memristor," *ACS nano* **5**, 7669–7676 (2011).
- ²M. Lanza, A. Sebastian, W. D. Lu, M. Le Gallo, M.-F. Chang, D. Akinwande, F. M. Puglisi, H. N. Alshareef, M. Liu, and J. B. Roldan, "Memristive technologies for data storage, computation, encryption, and radio-frequency communication," *Science* **376**, eabj9979 (2022).
- ³S. Bertolazzi, P. Bondavalli, S. Roche, T. San, S. Choi, L. Colombo, F. Bonaccorso, and P. Samori, "Nonvolatile Memories Based on Graphene and Related 2D Materials," **31**, 1806663.
- ⁴C.-C. Chiang, V. Ostwal, P. Wu, C.-S. Pang, F. Zhang, Z. Chen, and J. Appenzeller, "Memory applications from 2D materials," **8**, 021306.
- ⁵Y. Li, Z. Wang, R. Midya, Q. Xia, and J. J. Yang, "Review of memristor devices in neuromorphic computing: materials sciences and device challenges," *Journal of Physics D: Applied Physics* **51**, 503002 (2018).
- ⁶C. Tan, Z. Liu, W. Huang, and H. Zhang, "Non-volatile resistive memory devices based on solution-processed ultrathin two-dimensional nanomaterials," *Chemical society reviews* **44**, 2615–2628 (2015).
- ⁷C. Hao, F. Wen, J. Xiang, S. Yuan, B. Yang, L. Li, W. Wang, Z. Zeng, L. Wang, Z. Liu, *et al.*, "Liquid-exfoliated black phosphorous nanosheet thin films for flexible resistive random access memory applications," *Advanced Functional Materials* **26**, 2016–2024 (2016).
- ⁸X. Wu, R. Ge, P.-A. Chen, H. Chou, Z. Zhang, Y. Zhang, S. Banerjee, M.-H. Chiang, J. C. Lee, and D. Akinwande, "Thinnest Nonvolatile Memory Based on Monolayer h-BN," **31**, 1806790.
- ⁹A. A. Bessonov, M. N. Kirikova, D. I. Petukhov, M. Allen, T. Ryhänen, and M. J. Bailey, "Layered memristive and memcapacitive switches for printable electronics," *Nature materials* **14**, 199–204 (2015).
- ¹⁰D. Son, S. I. Chae, M. Kim, M. K. Choi, J. Yang, K. Park, V. S. Kale, J. H. Koo, C. Choi, M. Lee, *et al.*, "Colloidal synthesis of uniform-sized molybdenum disulfide nanosheets for wafer-scale flexible nonvolatile memory," *Advanced materials* **28**, 9326–9332 (2016).
- ¹¹R. Ge, X. Wu, L. Liang, S. M. Hus, Y. Gu, E. Okogbue, H. Chou, J. Shi, Y. Zhang, S. K. Banerjee, *et al.*, "A library of atomically thin 2d materials featuring the conductive-point resistive switching phenomenon," *Advanced Materials* **33**, 2007792 (2021).
- ¹²R. Ge, X. Wu, M. Kim, J. Shi, S. Sonde, L. Tao, Y. Zhang, J. C. Lee, and D. Akinwande, "Atomristor: nonvolatile resistance switching in atomic sheets of transition metal dichalcogenides," *Nano letters* **18**, 434–441 (2018).
- ¹³D.-H. Kwon, K. M. Kim, J. H. Jang, J. M. Jeon, M. H. Lee, G. H. Kim, X.-S. Li, G.-S. Park, B. Lee, S. Han, *et al.*, "Atomic structure of conducting nanofilaments in tio2 resistive switching memory," *Nature nanotechnology* **5**, 148–153 (2010).
- ¹⁴J. Yao, Z. Sun, L. Zhong, D. Natelson, and J. M. Tour, "Resistive switches and memories from silicon oxide," *Nano letters* **10**, 4105–4110 (2010).
- ¹⁵S. M. Hus, R. Ge, P.-A. Chen, L. Liang, G. E. Donnelly, W. Ko, F. Huang, M.-H. Chiang, A.-P. Li, and D. Akinwande, "Observation of single-defect memristor in an mos2 atomic sheet," *Nature Nanotechnology* **16**, 58–62 (2021).
- ¹⁶H. Qiu, T. Xu, Z. Wang, W. Ren, H. Nan, Z. Ni, Q. Chen, S. Yuan, F. Miao, F. Song, *et al.*, "Hopping transport through defect-induced localized states in molybdenum disulphide," *Nature communications* **4**, 2642 (2013).
- ¹⁷D. Jena and A. Konar, "Enhancement of carrier mobility in semiconductor nanostructures by dielectric engineering," *Physical review letters* **98**, 136805 (2007).
- ¹⁸S. Tongay, J. Suh, C. Ataca, W. Fan, A. Luce, J. S. Kang, J. Liu, C. Ko, R. Raghunathanan, J. Zhou, *et al.*, "Defects activated photoluminescence in two-dimensional semiconductors: interplay between bound, charged and free excitons," *Scientific reports* **3**, 2657 (2013).
- ¹⁹T. Korn, S. Heydrich, M. Hirmer, J. Schmutzler, and C. Schüller, "Low-temperature photocarrier dynamics in monolayer mos2," *Applied Physics Letters* **99** (2011).
- ²⁰S. W. Han, Y. H. Hwang, S.-H. Kim, W. S. Yun, J. D. Lee, M. G. Park, S. Ryu, J. S. Park, D.-H. Yoo, S.-P. Yoon, *et al.*, "Controlling ferromagnetic easy axis in a layered mos 2 single crystal," *Physical review letters* **110**, 247201 (2013).
- ²¹M. Zhang, Q. Li, W. Cheng, Y. Gao, B. Liao, and M. Ying, "Robust room-temperature ferromagnetism induced by defect engineering in monolayer mos2," *Applied Surface Science* **608**, 155220 (2023).
- ²²F. Tumino, C. S. Casari, A. Li Bassi, and S. Tosoni, "Nature of point defects in single-layer mos2 supported on au (111)," *The Journal of Physical Chemistry C* **124**, 12424–12431 (2020).
- ²³X.-D. Li, B.-Q. Wang, N.-K. Chen, and X.-B. Li, "Resistive switching mechanism of mos2 based atomristor," *Nanotechnology* **34**, 205201 (2023).
- ²⁴G. Boschetto, S. Carapezzi, C. Delacour, M. Abernot, T. Gil, and A. Todri-Sanial, "Ab initio computer simulations on interfacial properties of single-layer mos2 and au contacts for two-dimensional nanodevices," *ACS Applied Nano Materials* **5**, 10192–10202 (2022).
- ²⁵G. Boschetto, S. Carapezzi, and A. Todri-Sanial, "Non-volatile resistive switching mechanism in single-layer mos 2 memristors: Insights from ab initio modelling of au and mos 2 interfaces," *Nanoscale Advances* (2023).
- ²⁶S. Yasuda, R. Takahashi, R. Osaka, R. Kumagai, Y. Miyata, S. Okada, Y. Hayamizu, and K. Murakoshi, "Out-of-plane strain induced in a moiré superstructure of monolayer mos2 and mose2 on au (111)," *Small* **13**,

- 1700748 (2017).
- ²⁷S. McDonnell, R. Addou, C. Buie, R. M. Wallace, and C. L. Hinkle, "Defect-dominated doping and contact resistance in mos₂," *ACS nano* **8**, 2880–2888 (2014).
 - ²⁸M. Cook, R. Palandech, K. Doore, Z. Ye, G. Ye, R. He, and A. J. Stollenwerk, "Influence of interface coupling on the electronic properties of the au/mos₂ junction," *Physical Review B* **92**, 201302 (2015).
 - ²⁹A. Carladous, R. Coratger, F. Ajustron, G. Seine, R. Péchou, and J. Beauvillain, "Light emission from spectral analysis of au/mos₂ nanocontacts stimulated by scanning tunneling microscopy," *Physical Review B* **66**, 045401 (2002).
 - ³⁰A. Bruix, J. A. Miwa, N. Hauptmann, D. Wegner, S. Ulstrup, S. S. Grønborg, C. E. Sanders, M. Dendzik, A. G. Čabo, M. Bianchi, *et al.*, "Single-layer mos₂ on au (111): Band gap renormalization and substrate interaction," *Physical Review B* **93**, 165422 (2016).
 - ³¹C. Gong, C. Huang, J. Miller, L. Cheng, Y. Hao, D. Cobden, J. Kim, R. S. Ruoff, R. M. Wallace, K. Cho, *et al.*, "Metal contacts on physical vapor deposited monolayer mos₂," *ACS nano* **7**, 11350–11357 (2013).
 - ³²A. Bruix, H. G. Fuchtbauer, A. K. Tuxen, A. S. Walton, M. Andersen, S. Porsgaard, F. Besenbacher, B. Hammer, and J. V. Lauritsen, "In situ detection of active edge sites in single-layer mos₂ catalysts," *ACS nano* **9**, 9322–9330 (2015).
 - ³³M. Velický, G. E. Donnelly, W. R. Hendren, S. McFarland, D. Scullion, W. J. I. DeBenedetti, G. C. Correa, Y. Han, A. J. Wain, M. A. Hines, D. A. Muller, K. S. Novoselov, H. D. Abruña, R. M. Bowman, E. J. G. Santos, and F. Huang, "Mechanism of Gold-Assisted Exfoliation of Centimeter-Sized Transition-Metal Dichalcogenide Monolayers," **12**, 10463–10472.
 - ³⁴T. Ozaki, "Variationally optimized atomic orbitals for large-scale electronic structures," *Physical Review B* **67**, 155108 (2003).
 - ³⁵T. Ozaki and H. Kino, "Efficient projector expansion for the ab initio lcao method," *Physical Review B* **72**, 045121 (2005).
 - ³⁶K. Lejaeghere, G. Bihlmayer, T. Björkman, P. Blaha, S. Blügel, V. Blum, D. Caliste, I. E. Castelli, S. J. Clark, A. Dal Corso, *et al.*, "Reproducibility in density functional theory calculations of solids," *Science* **351**, aad3000 (2016).
 - ³⁷I. Morrison, D. Bylander, and L. Kleinman, "Nonlocal hermitian norm-conserving vanderbilt pseudopotential," *Physical Review B* **47**, 6728 (1993).
 - ³⁸J. P. Perdew, K. Burke, and M. Ernzerhof, "Generalized gradient approximation made simple," *Physical review letters* **77**, 3865 (1996).
 - ³⁹S. Grimme, S. Ehrlich, and L. Goerigk, "Effect of the damping function in dispersion corrected density functional theory," *Journal of computational chemistry* **32**, 1456–1465 (2011).
 - ⁴⁰M. Otani and O. Sugino, "First-principles calculations of charged surfaces and interfaces: A plane-wave nonrepeated slab approach," *Physical Review B* **73**, 115407 (2006).
 - ⁴¹C.-C. Lee, Y. Yamada-Takamura, and T. Ozaki, "Unfolding method for first-principles lcao electronic structure calculations," *Journal of Physics: Condensed Matter* **25**, 345501 (2013).
 - ⁴²M. Otani and O. Sugino, "First-principles calculations of charged surfaces and interfaces: A plane-wave nonrepeated slab approach," *Physical Review B* **73**, 115407 (2006).
 - ⁴³A. Jain, S. P. Ong, G. Hautier, W. Chen, W. D. Richards, S. Dacek, S. Cholia, D. Gunter, D. Skinner, G. Ceder, and K. A. Persson, "Commentary: The Materials Project: A materials genome approach to accelerating materials innovation," **1**, 011002.
 - ⁴⁴C. Freysoldt, B. Grabowski, T. Hickel, J. Neugebauer, G. Kresse, A. Janotti, and C. G. Van de Walle, "First-principles calculations for point defects in solids," **86**, 253–305.
 - ⁴⁵G. K. Madsen and D. J. Singh, "Boltztrap. a code for calculating band-structure dependent quantities," *Computer Physics Communications* **175**, 67–71 (2006).
 - ⁴⁶Z. Jin, Q. Liao, H. Fang, Z. Liu, W. Liu, Z. Ding, T. Luo, and N. Yang, "A revisit to high thermoelectric performance of single-layer mos₂," *Scientific reports* **5**, 18342 (2015).
 - ⁴⁷H. Guo, T. Yang, P. Tao, Y. Wang, and Z. Zhang, "High pressure effect on structure, electronic structure, and thermoelectric properties of mos₂," *Journal of Applied Physics* **113** (2013).
 - ⁴⁸S. Poncé, F. Macheda, E. R. Margine, N. Marzari, N. Bonini, and F. Giustino, "First-principles predictions of hall and drift mobilities in semiconductors," *Physical Review Research* **3**, 043022 (2021).
 - ⁴⁹A. M. Ganose, J. Park, A. Faghaninia, R. Woods-Robinson, K. A. Persson, and A. Jain, "Efficient calculation of carrier scattering rates from first principles," *Nature communications* **12**, 2222 (2021).
 - ⁵⁰S. Bhattacharyya, T. Pandey, and A. K. Singh, "Effect of strain on electronic and thermoelectric properties of few layers to bulk mos₂," *Nanotechnology* **25**, 465701 (2014).
 - ⁵¹K.-A. Min, J. Park, R. M. Wallace, K. Cho, and S. Hong, "Reduction of fermi level pinning at au–mos₂ interfaces by atomic passivation on au surface," *2D Materials* **4**, 015019 (2016).
 - ⁵²J. Kang, W. Liu, D. Sarkar, D. Jena, and K. Banerjee, "Computational study of metal contacts to monolayer transition-metal dichalcogenide semiconductors," *Physical Review X* **4**, 031005 (2014).
 - ⁵³C. Gong, L. Colombo, R. M. Wallace, and K. Cho, "The unusual mechanism of partial fermi level pinning at metal–mos₂ interfaces," *Nano letters* **14**, 1714–1720 (2014).
 - ⁵⁴H.-P. Komsa and A. V. Krashennnikov, "Native defects in bulk and monolayer mos₂ from first principles," *Physical Review B* **91**, 125304 (2015).
 - ⁵⁵X.-D. Li, N.-K. Chen, B.-Q. Wang, and X.-B. Li, "Conductive mechanism in memristor at the thinnest limit: The case based on monolayer boron nitride," *Applied Physics Letters* **121** (2022).
 - ⁵⁶A. Ruban, B. Hammer, P. Stoltze, H. L. Skriver, and J. K. Nørskov, "Surface electronic structure and reactivity of transition and noble metals," *Journal of Molecular Catalysis A: Chemical* **115**, 421–429 (1997).
 - ⁵⁷S. Schnur and A. Groß, "Strain and coordination effects in the adsorption properties of early transition metals: A density-functional theory study," *Physical Review B* **81**, 033402 (2010).
 - ⁵⁸J. Bardeen, "Surface states and rectification at a metal semiconductor contact," *Physical review* **71**, 717 (1947).
 - ⁵⁹R. B. Darling, "Defect-state occupation, fermi-level pinning, and illumination effects on free semiconductor surfaces," *Physical Review B* **43**, 4071 (1991).
 - ⁶⁰V. Heine, "Theory of surface states," *Physical Review* **138**, A1689 (1965).
 - ⁶¹S. G. Louie and M. L. Cohen, "Self-consistent pseudopotential calculation for a metal-semiconductor interface," *Physical Review Letters* **35**, 866 (1975).
 - ⁶²H. Hasegawa and T. Sawada, "On the electrical properties of compound semiconductor interfaces in metal/insulator/semiconductor structures and the possible origin of interface states," *Thin Solid Films* **103**, 119–140 (1983).
 - ⁶³M. Choi, "Strain-enhanced p doping in monolayer mos₂," *Physical Review Applied* **9**, 024009 (2018).
 - ⁶⁴M. Velicky, A. Rodriguez, M. Bousa, A. V. Krayev, M. Vondracek, J. Honolka, M. Ahmadi, G. E. Donnelly, F. Huang, H. D. Abruña, *et al.*, "Strain and charge doping fingerprints of the strong interaction between monolayer mos₂ and gold," *The journal of physical chemistry letters* **11**, 6112–6118 (2020).
 - ⁶⁵A. Michail, N. Delikoukos, J. Parthenios, C. Galiotis, and K. Papagelis, "Optical detection of strain and doping inhomogeneities in single layer mos₂," *Applied Physics Letters* **108** (2016).

Supplemental Material:
Nature of point defects in monolayer MoS₂ and the MoS₂/(111)-Au heterojunction
 Roozbeh Anvari and Wennie Wang
 McKetta Department of Chemical Engineering, University of Texas at Austin

S1. POINT DEFECTS IN FREE-STANDING MONOLAYER MoS₂

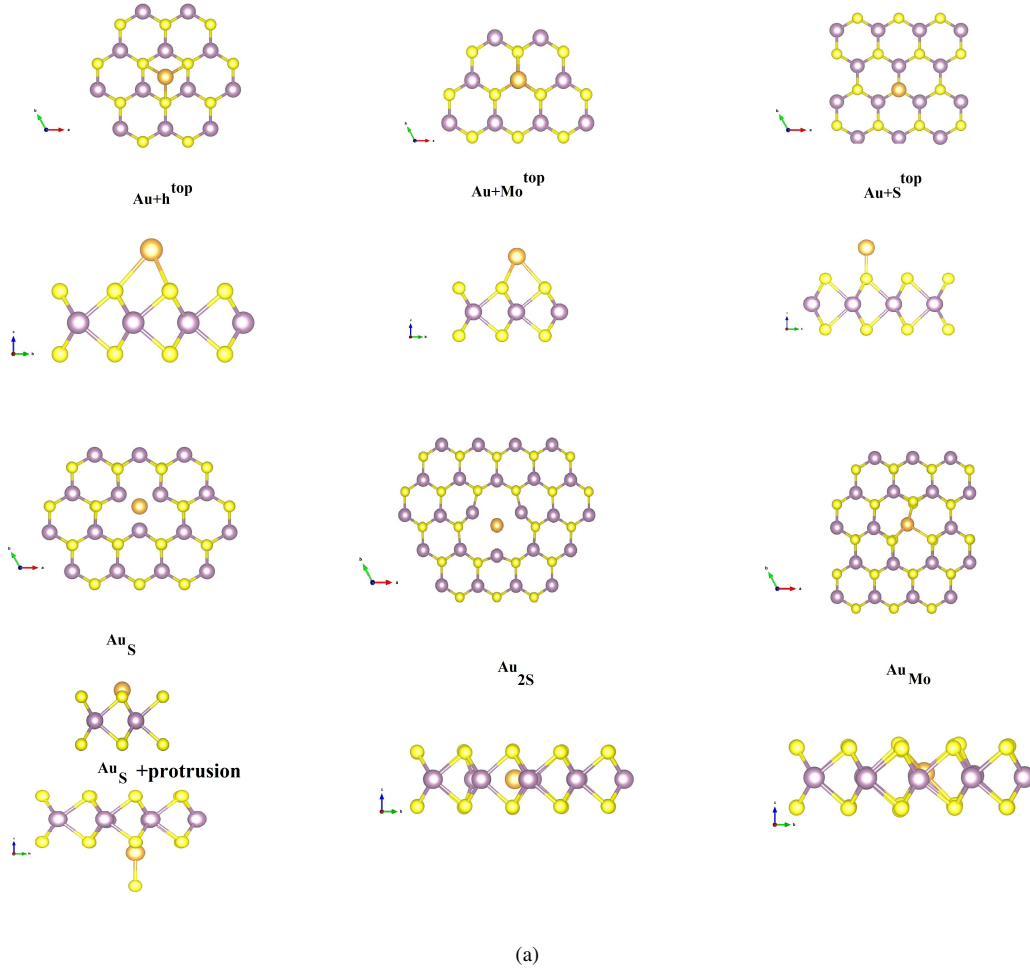


FIG. S1. Top and side-view of the studied stand-alone structures. The first two rows correspond to the top and side view of Au-atom adsorbed on top of the h-site ($Au + h^{top}$), Mo-top site ($Au + Mo^{top}$), and S-top site (Au_S). The third and fourth rows correspond to the top and side view of (Au_S) after protrusion, Au adsorbed into sulfur-divacancy (Au_{2S}), and Mo-vacancy (Au_{Mo}).

Figure S2 shows the fully relaxed atomic coordinates of the vertical (111)Au-MoS₂-(111)Au device, and the half (111)Au-MoS₂ system from the side and top. The calculated formation energy of a single sulfur vacancy (V_S) in (111)Au-MoS₂-(111)Au and (111)Au-MoS₂ heterostructures is 3.33 eV and 3.86 eV, respectively. The normal distance between S of MoS₂ and Au of the (111)-Au electrode is 2.897 (2.912 and 2.916) for the one (two)-sided heterostructure. As depicted in Figure S2a, the calculated electrostatic potential with respect to the vacuum level indicates that the interlayer distances, and the corresponding charge distribution are approximately identical between the full (111)Au-MoS₂-(111)Au heterostructure and the (111)Au-MoS₂ half system. Due to spatial and electrostatic symmetry of the (111)Au-MoS₂-(111)Au, we have focus on the characteristics of the half system MoS₂/(111)Au in this study.

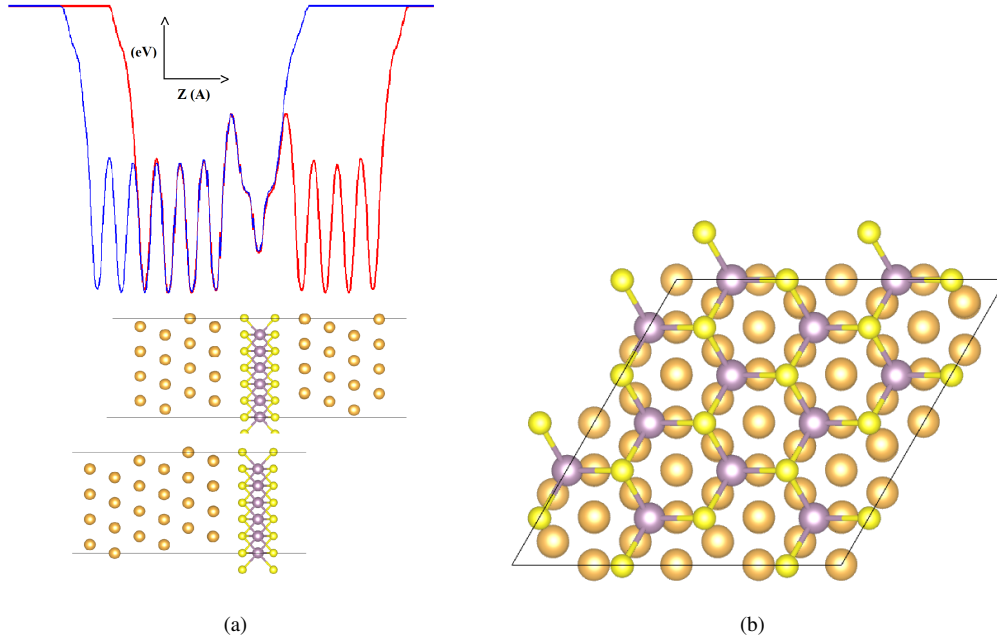


FIG. S2. (a) Side view of the Au(111)-MoS₂-Au(111) and Au(111)-MoS₂ structures, and the corresponding electrostatic potential relative to the vacuum level. (b) Top-view of the reconstructed $(2\sqrt{3} \times 2\sqrt{3}) - \text{MoS}_2$ layer.

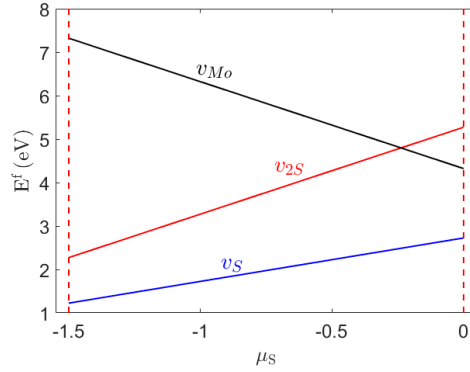


FIG. S3. Defect formation energy of the V_S , V_{2S} and V_{Mo} vacancy defects in stand-alone (no substrate) MoS₂ as a function of the chemical potential of sulfur. Chemical potentials are obtained from equilibrium of monolayer-MoS₂ with bulk Mo (solid) and solid phase S. Left and right boundaries correspond to the sulfur-poor and sulfur-rich environments, respectively.

structure	E^f	E^{ads}	E^b	E^f	E^{ads}	REF. ^{S54}	REF. ^{S22}
v_S	2.72			2.799		2.7	2.81
v_{2S}	5.27						5.44
v_{Mo}	4.32					3.6	2.22
Au + pr, htop	2.7	2.830			2.64		
Au + pr, Stop	2.7	2.831			2.69		
Au + pr, Motop	2.8	2.925			2.76		
Au _S	3.55	0.95	-1.87				
Au _{2S}	10.65	5.498	2.86				
Au _{Mo}}	4.17	-0.026	-2.95				

TABLE S1. Formation energy of vacancies (E^f), adsorption energy (E^{ads}), and binding energy (E^b) of Au+vacancy defect complexes (all in eV) in freestanding $(6 \times 6) - \text{MoS}_2$ supercell with no strain. The last 2 columns are calculated using Quantum Espresso for freestanding $(4 \times 4) - \text{MoS}_2$ supercell. Values are tabulated for sulfur-rich conditions.

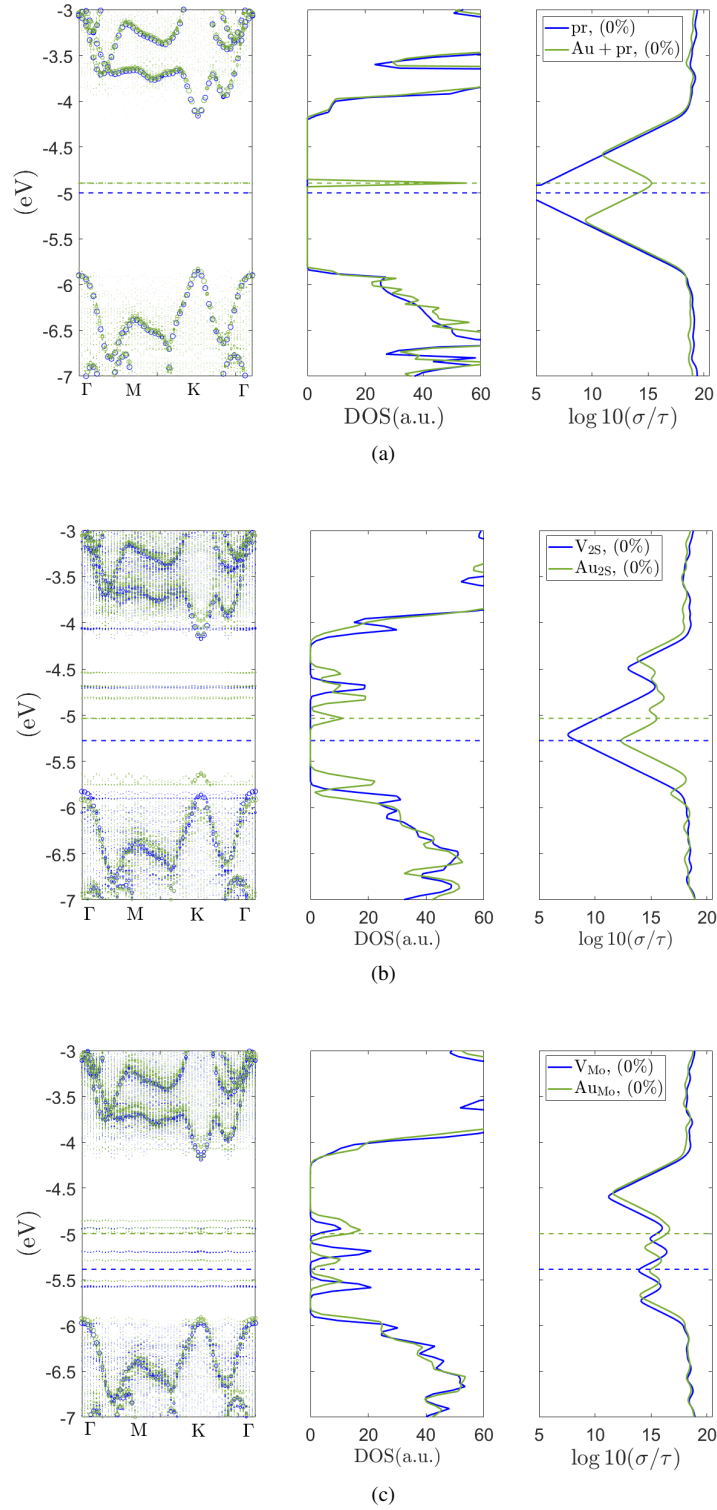
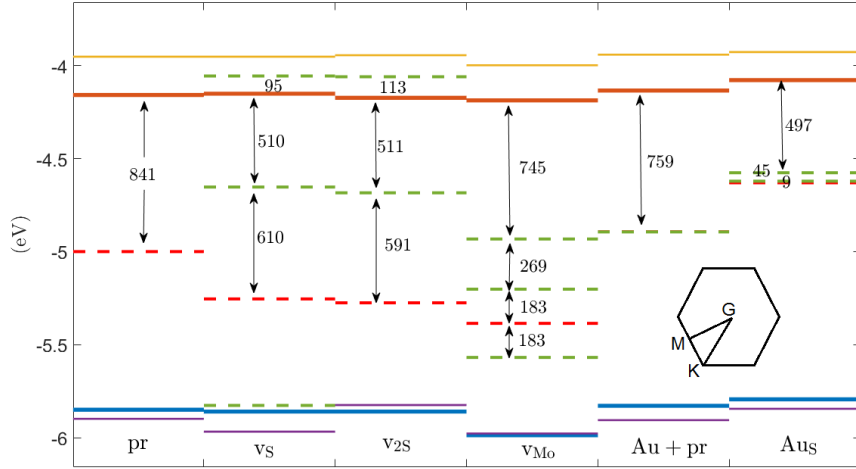


FIG. S4. Unfolded bandstructure (left), DOS (middle) and normalized electrical conductivity (right) of (6x6) supercell MoS₂ comparing the (a) pristine monolayer and Au adsorbed on the pristine monolayer, (b) sulfur divacancy and Au adsorbed on the sulfur divacancy, (c) molybdenum vacancy and Au adsorbed on the molybdenum vacancy, in blue and green, respectively. The dotted lines indicate the computed Fermi level.



(a)

FIG. S5. Energy diagram of the band edges of the free-standing monolayer without defects, with vacancies alone, and with Au+defect complexes. Solid orange and blue lines correspond to the conduction band minima and valence band maxima at the K-point, respectively. Solid gold and purple lines correspond to the conduction band minima and valence band maxima at the satellite valley next to CBM and Γ -point, respectively. Dashed red and dashed green lines correspond to the Fermi-level and defect levels, respectively. Numbers correspond to the energy difference between the levels indicated, in units of meV. As discussed in the main text, CBM and VBM of structure with zero strain are located at K-point. The valley that is presented in this figure is located along the K- Γ high symmetry line.

	σ_{xx}	σ_{zz}
V_S	7.851	5.53
V_{2S}	8.345	6.16
V_{Mo}	13.97	10.44
Au + pr	15.31	11.17
Au _S	15.57	11.53
Au _{2S}	15.52	11.47
Au _{Mo}}	16.42	12.91

TABLE S2. Calculated normalized conductivity ($\log_{10}(\sigma/\tau)$) using the constant time relaxation approximation and the Boltzmann transport equation of native defects of free-standing MoS₂ at the computed Fermi level.

S2. EFFECT OF STRAIN IN FREE-STANDING MoS_2

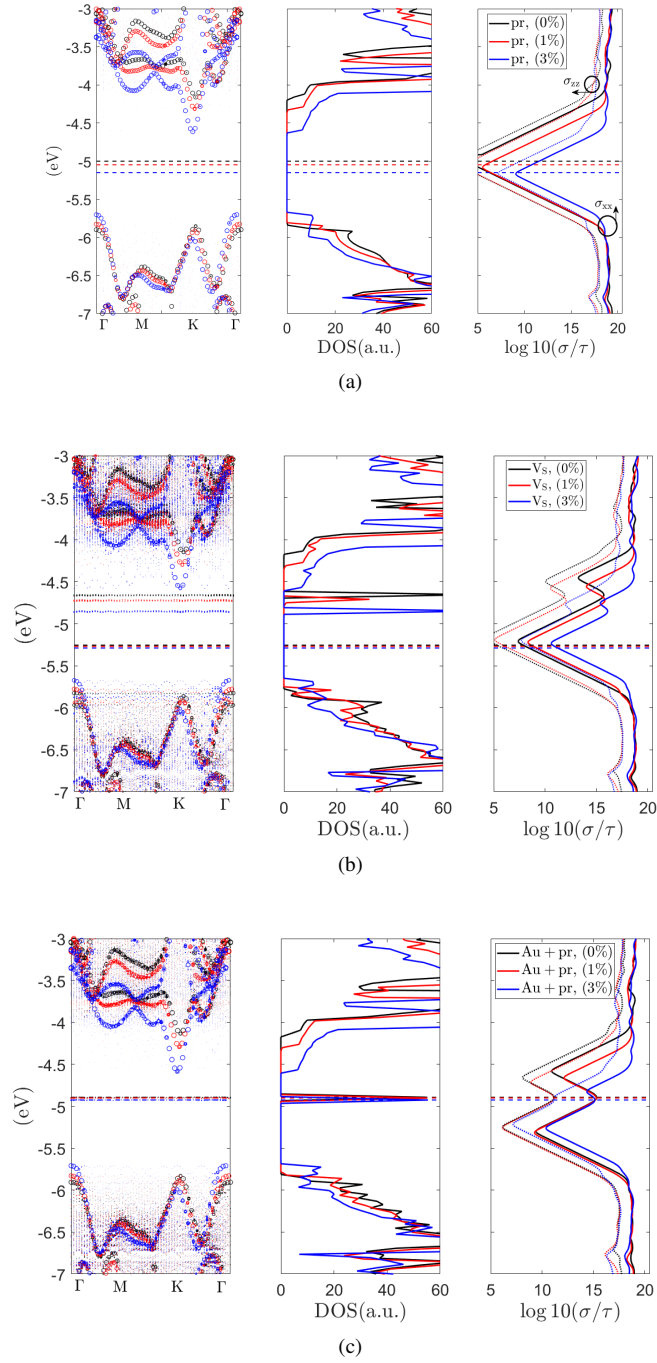


FIG. S6. Effect of biaxial tensile strain on the electronic structure and conductivity of (a) pristine MoS_2 , (b) MoS_2 with a sulfur vacancy, and (c) pristine MoS_2 with an Au adatom adsorbed.

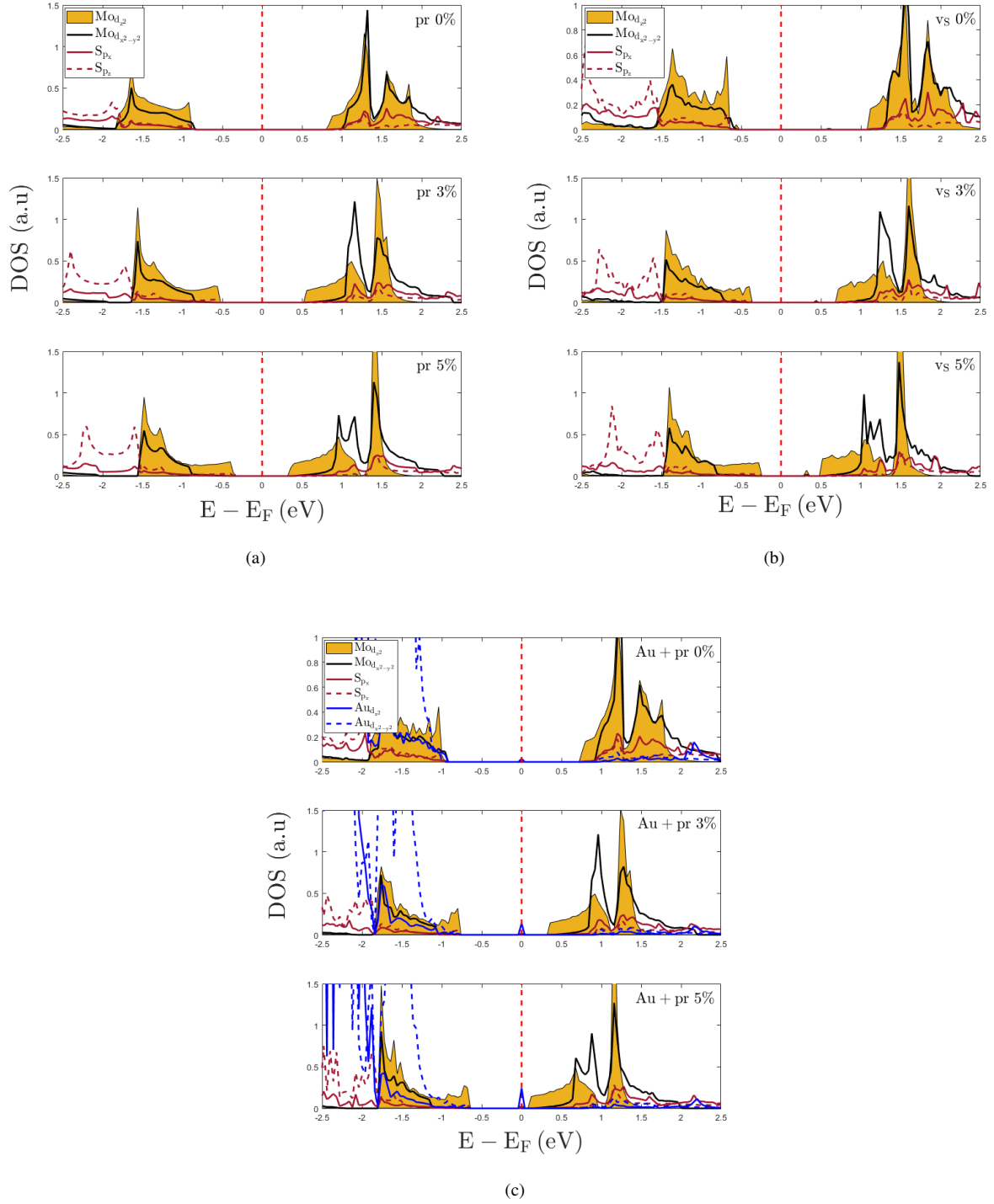


FIG. S7. Changes of the PDOS of free-standing MoS₂ structures with biaxial tensile strain. Changes of net charge accumulated on the Au adatom with strain indicates that Au is hybridizing differently with the host MoS₂ in Au+pr and Au_S structures. PDOS analysis indicates that the hybridization of Au in Au+pr is mainly d_{z^2} , while the main contribution of Au in Au_S is $d_{x^2-y^2}$.

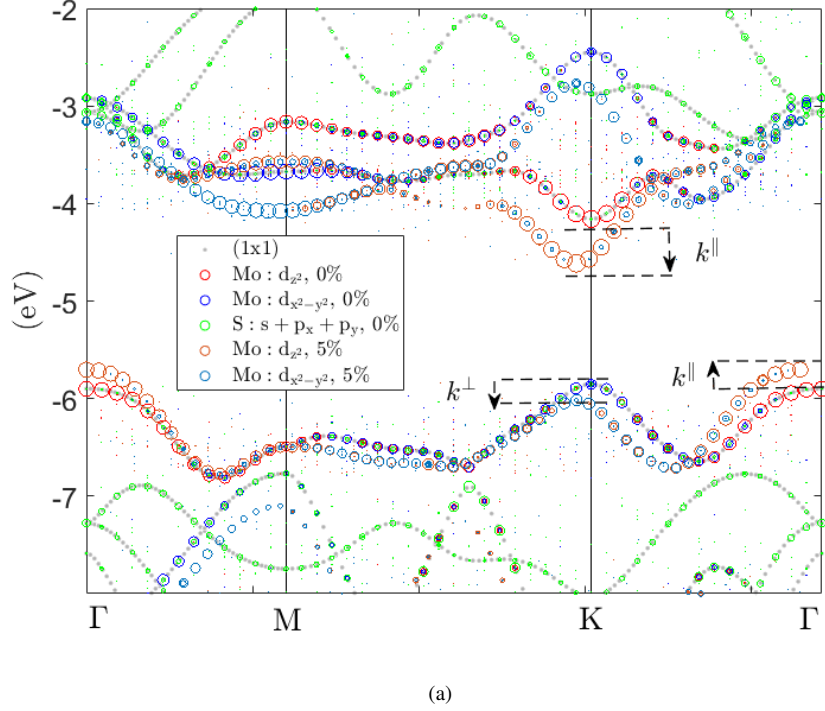


FIG. S8. Unfolded band structure of free standing (6x6)-MoS₂ structure under 0 and 5% tensile strain. The radius of the circles represent the magnitude of the spectral weight obtained by unfolding. Energy levels are relative to vacuum. Arrows indicates the direction of shift in energy with increasing tensile strain.

strain %	pr	vs	Au + pr	Aus
-1	-4.958	-5.223	-4.884	-4.564
0	-4.999	-5.254	-4.892	-4.630
1	-5.047	-5.269	-4.901	-4.701
2	-5.096	-5.278	-4.912	-4.778
3	-5.150	-5.288	-4.924	-4.858
4	-5.194	-5.299	-4.939	-4.939
5	-5.238	-5.314	-4.956	-5.022
6	-5.281	-5.331	-4.997	-5.105
7	-5.323	-5.354	-5.063	-5.188

TABLE S3. Changes of workfunction (in units of eV) of freestanding MoS₂ structures with biaxial strain.

strain %	d _S - d _{Mo}	d _S - d _{Mo}	d _{Au} - d _{Mo}	d _{z²} q/e	d _{x²-y²} q/e
-1	-1.5968	1.5963	3.7014	-0.0009	0.0007
0	-1.5860	1.5860	3.6703	0	0
1	-1.5763	1.5747	3.6376	0.0010	-0.0012
2	-1.5651	1.5664	3.6132	0.0019	-0.0021
3	-1.5558	1.5563	3.5786	0.0029	-0.0031
4	-1.5471	1.5465	3.5453	0.0039	-0.0048
5	-1.5395	1.5369	3.5063	0.0048	-0.0060
6	-1.5300	1.5291	3.4595	0.0062	-0.0071
7	-1.5201	1.5217	3.4070	0.0078	-0.0081

TABLE S4. (columns 2–4) Effect of biaxial strain on the interlayer distance of the plane of S and Au to that of Mo atoms of the freestanding (6x6)-Au + pr structure consisting of an Au adatom on a pristine monolayer of MoS₂; (columns 5–6) the corresponding change in the charge population of the d_{3z²-r²} and d_{x²-y²} orbitals of the Au-adatom of this structure with respect to those of 0% strain.

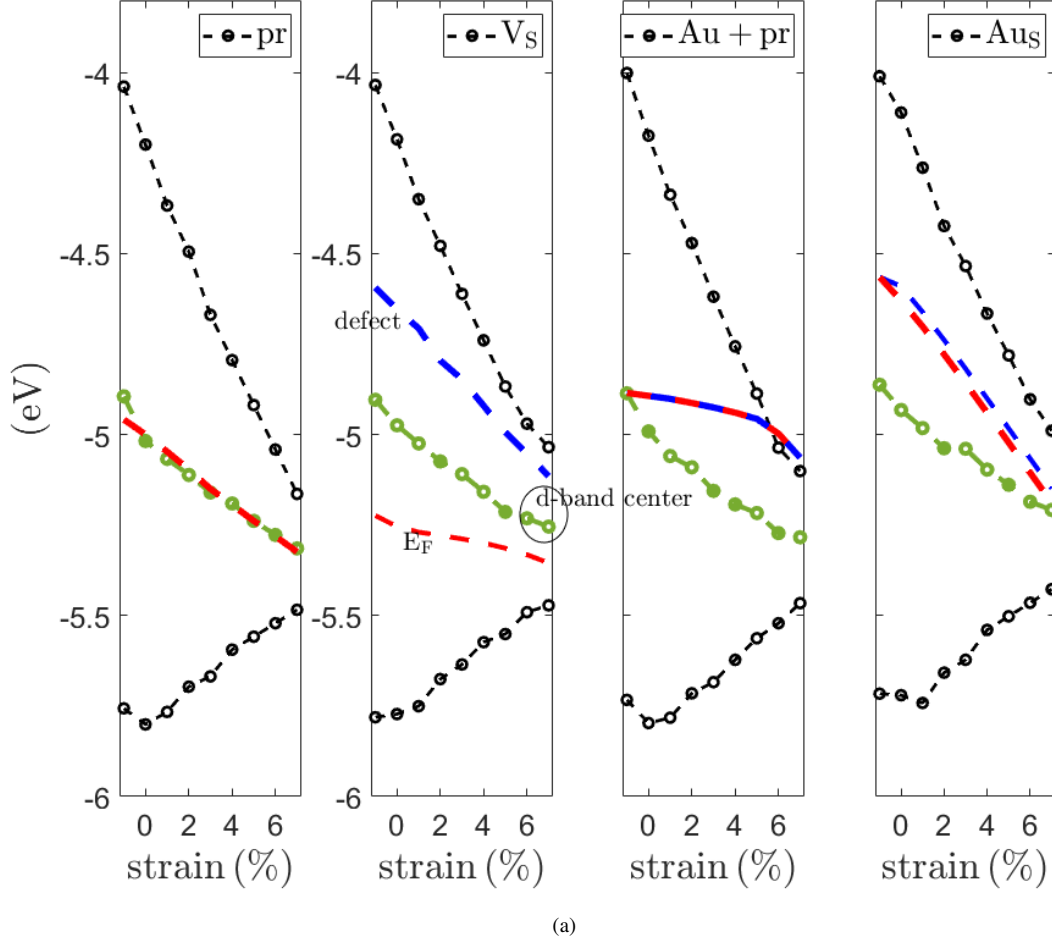


FIG. S9. Effect of strain on the band edges of freestanding structures.

strain %	$d_S - d_{Mo}$	$d_S - d_{Mo}$	$d_{Au} - d_{Mo}$	$d_{3z^2-r^2}$ q/e	$d_{x^2-y^2}$ q/e
-1.0000	-1.5957	1.5962	2.0291	-0.0018	0.0001
0	-1.5865	1.5839	2.0099	0	0
1.0000	-1.5758	1.5745	1.9856	0.0014	0.0002
2.0000	-1.5666	1.5640	1.9650	0.0025	-0.0006
3.0000	-1.5556	1.5559	1.9479	0.0038	-0.0013
4.0000	-1.5463	1.5470	1.9206	0.0053	-0.0023
5.0000	-1.5369	1.5385	1.9047	0.0070	-0.0032
6.0000	-1.5288	1.5297	1.8821	0.0089	-0.0041
7.0000	-1.5197	1.5223	1.8631	0.0109	-0.0049

TABLE S5. (columns 2–4) Effect of biaxial strain on the interlayer distance of the plane of S and Au to that of Mo atoms of the freestanding (6x6)-AuS structure consisting of an Au adatom adsorbed on a sulfur vacancy site; (columns 5–6) the corresponding change in the charge population of the $d_{3z^2-r^2}$ and $d_{x^2-y^2}$ orbitals of the Au-adatom of this structure with respect to those of 0% strain.

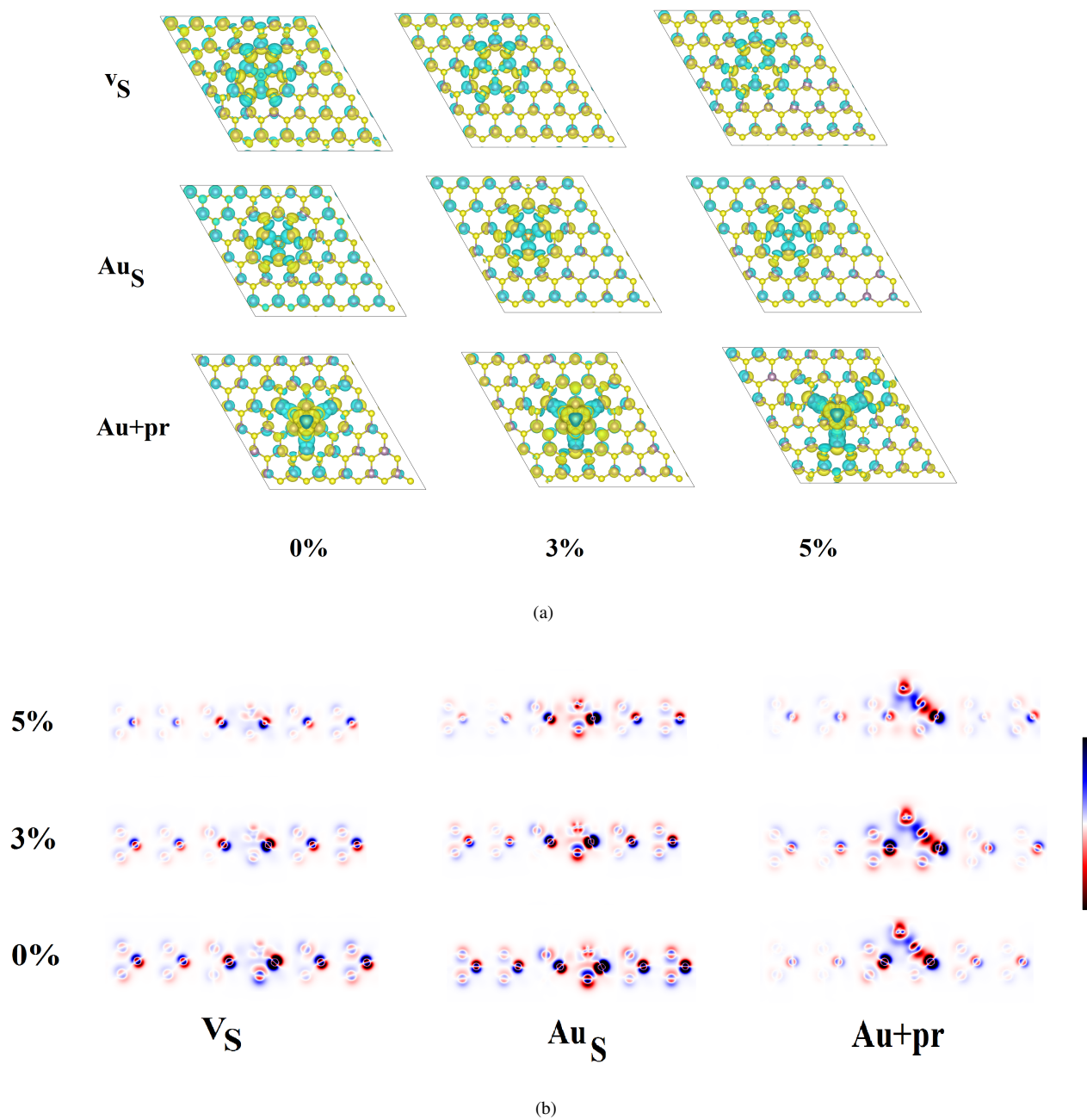


FIG. S10. (a) Charge difference profiles for free standing MoS₂ structures. Green represents charge depletion, yellow represents charge accumulation. (a) top view and (b) side view. Blue represents charge accumulation, red represents charge depletion.

$\varepsilon\%$	pr	V_S	Au + pr	Au _S
-1	-	18.46	35.23	35.42
0	-	18.90	35.19	35.93
1	13.41	20.46	35.18	36.44
2	17.39	23.33	34.84	36.87
3	21.13	25.80	34.79	37.48
4	24.70	28.21	34.78	37.99
5	28.26	30.53	37.68	38.53
6	31.17	32.72	40.15	38.03
7	34.12	35.14	41.34	39.57

TABLE S6. Calculated normalized conductivity ($\log_{10}(\sigma/\tau)$) of freestanding MoS₂ under biaxial strain at the computed Fermi-level, ($\pm\varepsilon$ and 0 correspond to tensile/compressive and no strain, respectively) calculated using constant time relaxation approximation and the Boltzmann transport equation.

S3. EFFECT OF STRAIN ON HETEROSTRUCTURE OF $\text{MoS}_2/(\text{111})\text{-Au}$

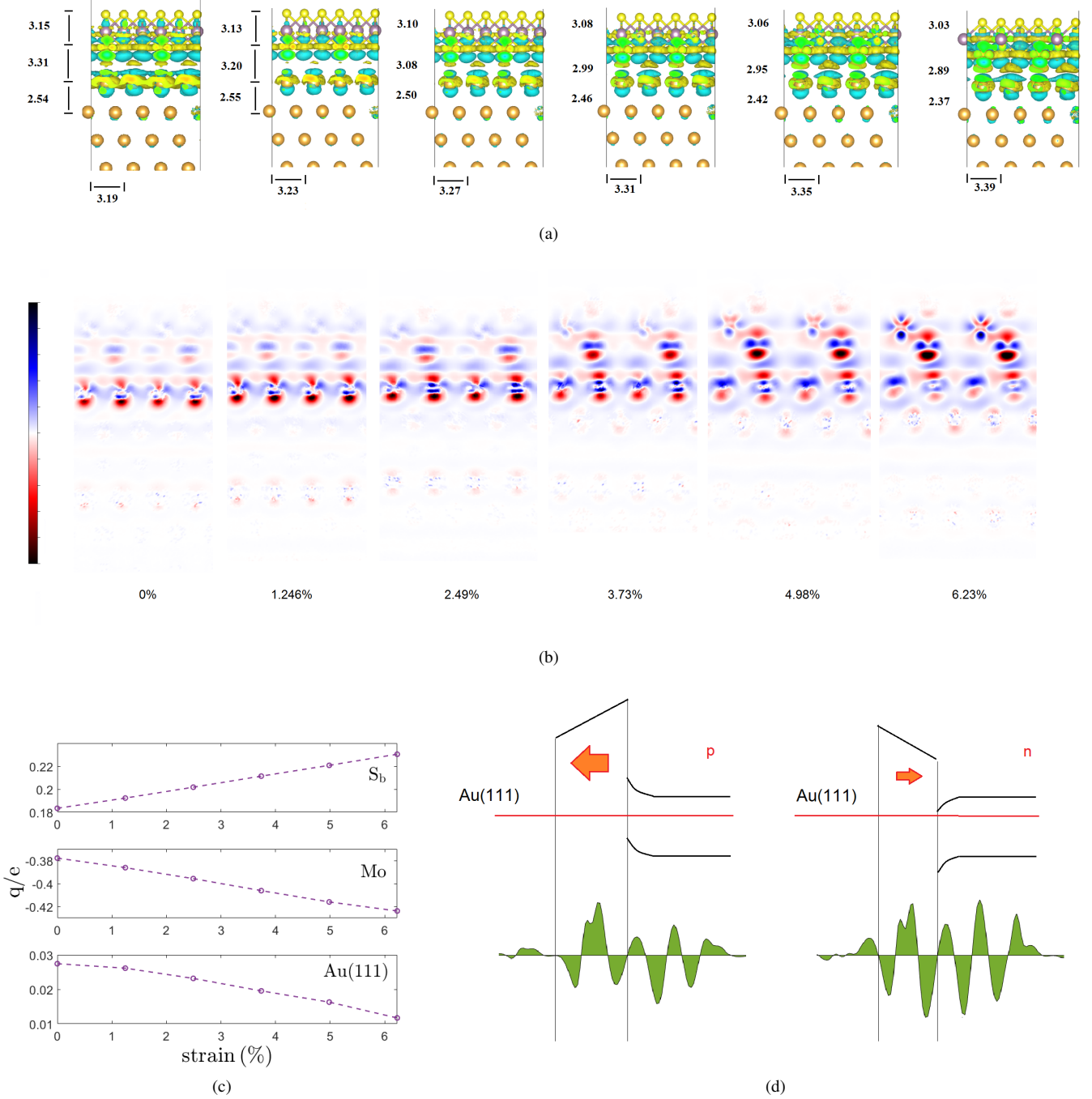


FIG. S11. (a) Charge difference plot and interlayer distances due to biaxial strain caused by lattice mismatch of the top MoS_2 layer with the (111)-Au substrate. The charge difference is obtained by $\rho_{\text{heterostructure}} - \rho_{\text{Au(111)}} - \rho_{\text{MoS}_2}$. Biaxial tensile strain increases from most left structure with top layer at 0% strain (supercell consists of lattice coordinates of stand-alone MoS_2), to the most right structure with top layer at 6.23% strain (lattice coordinates of (111)-Au). (b) Changes of the lattice vector constants and interlayer distances with increasing strain. (c) Mulliken charge analysis for the interfacial atoms forming the Mo-S-Au bonds. (d) Schematic (dimensions not to scale) demonstrates the effect of charge accumulation/depletion on the direction of interfacial dipole moment and corresponding changes of barrier height, and local band bending in the semiconductor. Variation of the interlayer distance and strain across the heterostructure cause local regions with different charge doping.

Here, we describe the change in the electronic structure of the $\text{Mo}_2/(\text{1110})\text{-Au}$ heterostructure with strain. Similar to free-

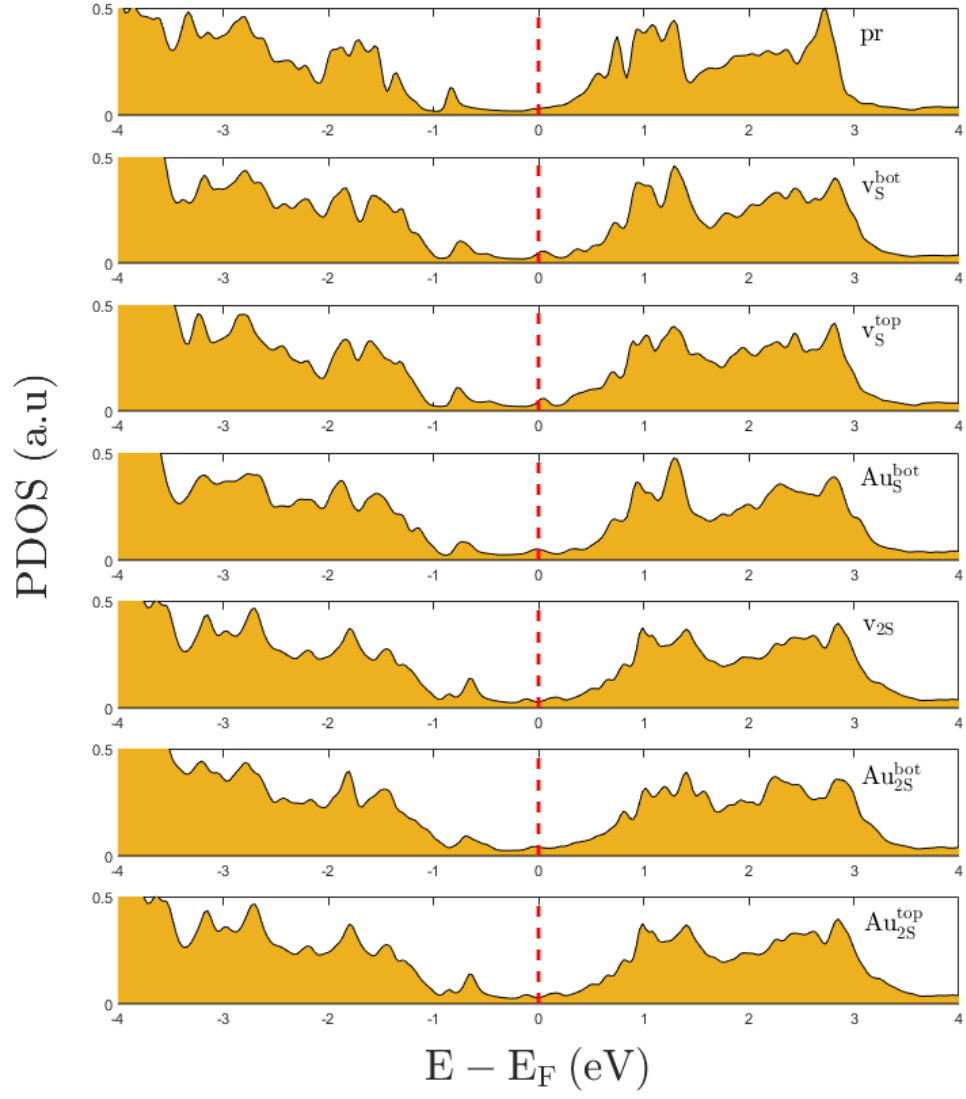
structure	Mo	Au _{ads}	S _{top}	S _{bot}	(111)Au _{surf}
$v_{Au}^{Mo} + Au_{2S}^{bot}$	0	-2.04	1.53	-1.45	-4.10
$v_{Au}^S + Au_{2S}^{bot}$	0	-2.07	1.58	-1.45	-4.1
Au_{2S}^{top}	0	1.86	1.49	-1.54	-4.72
Au_{2S}^{bot}	0	-2.04	1.54	-1.51	-4.36
Au_S^{top}	0	1.82	1.52	-1.40	-4.37
Au_S^{bot}	0	-2.02	1.54	-1.46	-4.26

TABLE S7. Atomic coordinates of Au+vacancy defect complexes in the MoS₂/(111)-Au heterostructure with lattice coordinates of the substrate (6.23% biaxial strain). Coordinates are taken relative to the plane of Mo-atoms. In all cases, Au^{top} is located approximately 0.36 Å above the plane of S^{top} atoms, Au^{bot} is located approximately 0.5 Å below the S^{bot} atoms; the interlayer distance between MoS₂ and (111)-Au is 2.9 Å.

structure	0 %	1.24 %	6.23 %	6.23 % , 2 elect.
v_S	3.95	5.43	3.86	3.34
Au_S^{bot}	-0.71	-2.14	-0.77	
Au_S^{top}			0.081	
$Au_S^{bot} + v_{Au}^S$		-0.77	-0.50	
$Au_S^{bot} + v_{Au}^{Mo}$	0.58		-0.48	
v_{2S}	8.38	8.87	8.03	7.01
Au_{2S}^{bot}	-1.21	0.092	-1.10	
Au_{2S}^{top}			-0.065	
$Au_{2S}^{bot} + v_{Au}^S$			-0.662	
$Au_{2S}^{bot} + v_{Au}^{Mo}$	-0.41		-0.756	
$Au_{2S}^{top} + v_{Au}^{Mo}$			0.252	

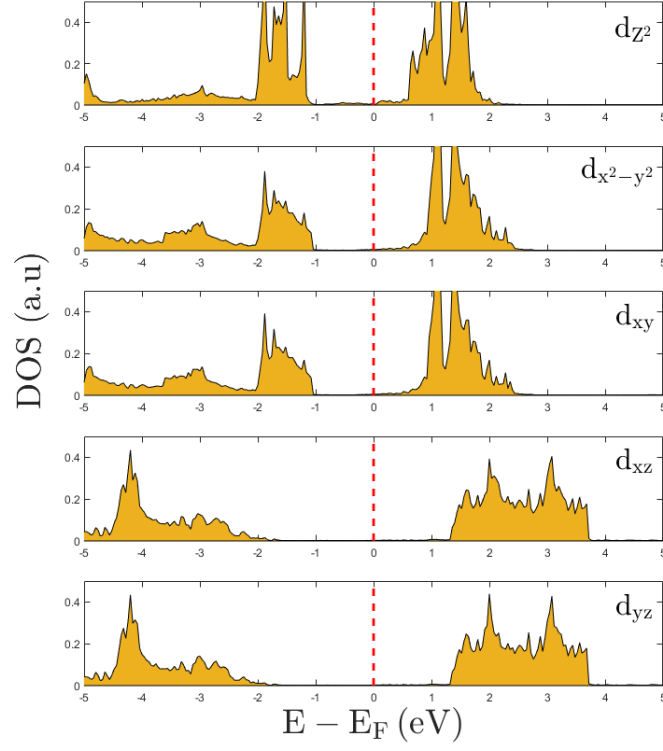
TABLE S8. Calculated formation energies of vacancies (left side of each column) and adsorption energy of Au+vacancy defect complexes in the MoS₂/(111)-Au heterostructure under 0 %, 1.24%, 6.23% biaxial strain. The last column corresponds to the Au(111)/MoS₂/Au(111) structure under 6.23 % tensile strain. The notation V_{Au}^X corresponds to a Au vacancy on the surface of the electrode under atom X=Mo, S of the MoS₂.

standing MoS₂, the VBM and CBM contain by Mo: $d_{x^2-y^2}$ and Mo: d_{z^2} character, respectively, under no strain. The peak of the Mo: $d_{x^2-y^2}$ states that is located 200 meV below VBM eventually shifts up and splits from the VBM in biaxially strained structures. In the V_S structure, the defect level induced by V_S is located approximately 0.4 eV below the CBM. This defect level mainly consists of S orbitals marginally mixing with Mo orbitals. The peak of this defect level gets slightly closer to the Fermi level by 40 meV as the Au_S structure forms and mainly consists of S and Au with a marginally contribution from Mo. The general trends are the same for Au_S+V_{2S} structure. As the Au_{2S} defect complex forms, multiple peaks arise in the band gap, located at -0.56, -0.12, 0.12 and 0.68 eV, relative to the Fermi level.

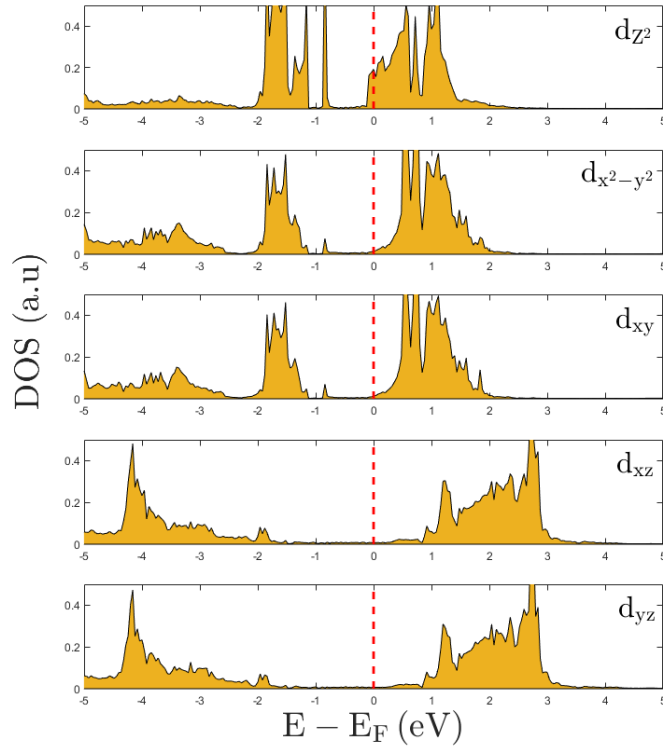


(a)

FIG. S12. Electronic structure (PDOS) of bottom S atom in various Au+defect structures in the MoS₂/(111)-Au heterostructure complex.



(a)



(b)

FIG. S13. Changes of d -orbitals of Mo in the MoS₂/(111)-Au heterostructure under (a) 0% and (b) 6.23% biaxial tensile strain. As discussed in the main text, the d -bands of the Mo shift downward with increasing strain. The band edges and gap energy levels are dominated by d_{z^2} and $d_{x^2-y^2}$ orbitals.

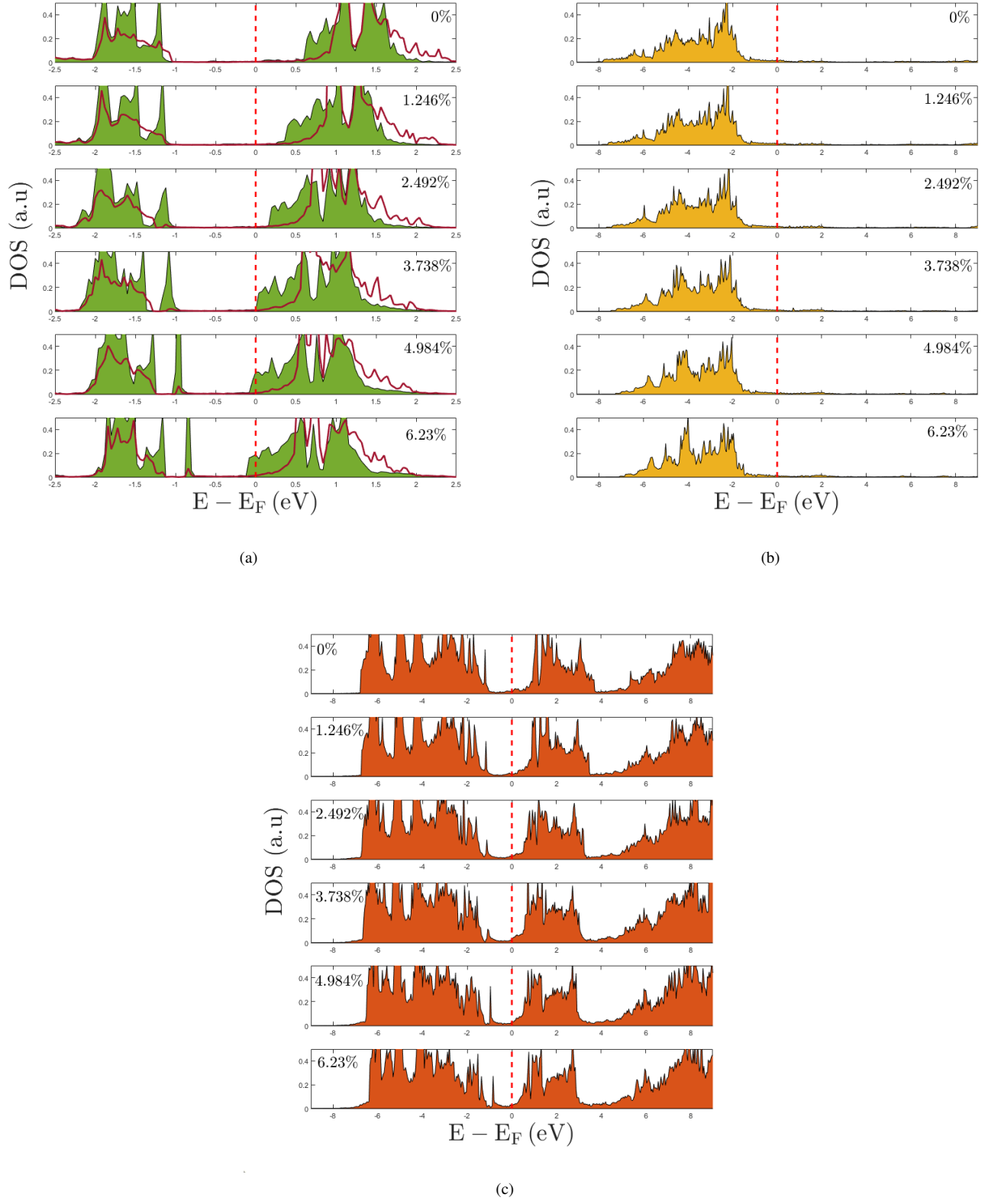


FIG. S14. Combined effect of heterostructure formation and strain on the d_{z^2} (green) $d_{x^2-y^2}$ (red) orbital of Mo (a), d_{z^2} -band of interfacial Au or the electrode (b) and all bands of interfacial S (c) in $\text{MoS}_2/(111)\text{-Au}$ heterostructure. Legend corresponds to the biaxial tensile strain in MoS_2 , and the Fermi-level is indicated by red dashed line. The center of the d-band of Mo significantly downshifts with increasing strain. On the contrary, the width and location of peaks of bands of interfacial Au and S atoms are not affected as significantly.

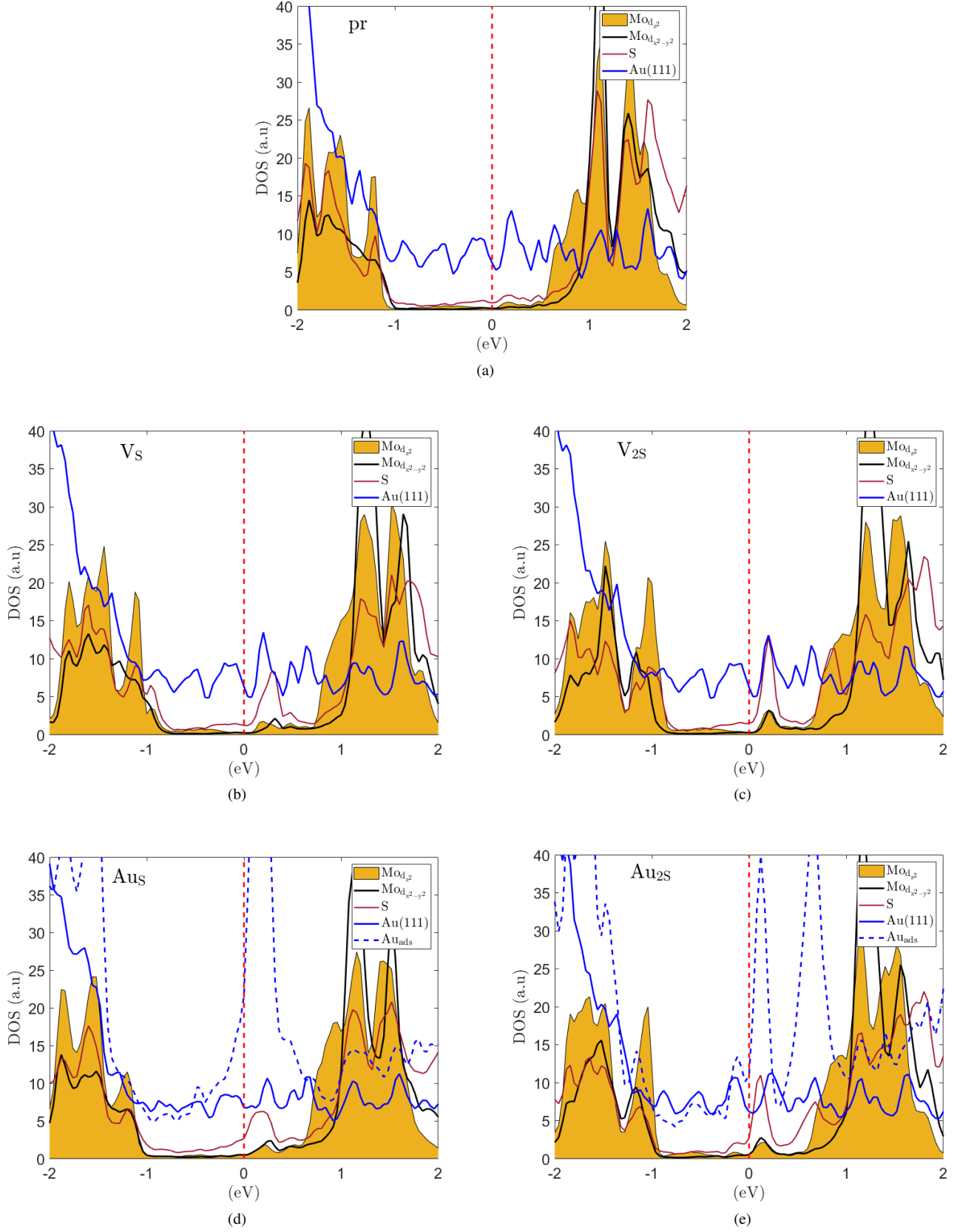


FIG. S15. PDOS of defect complexes in MoS₂/Au(111) heterostructure under 0 % biaxial strain. PDOS of Mo, S and Au_{ads} are multiplied by 50, 50 and 100, respectively for ease of eye.

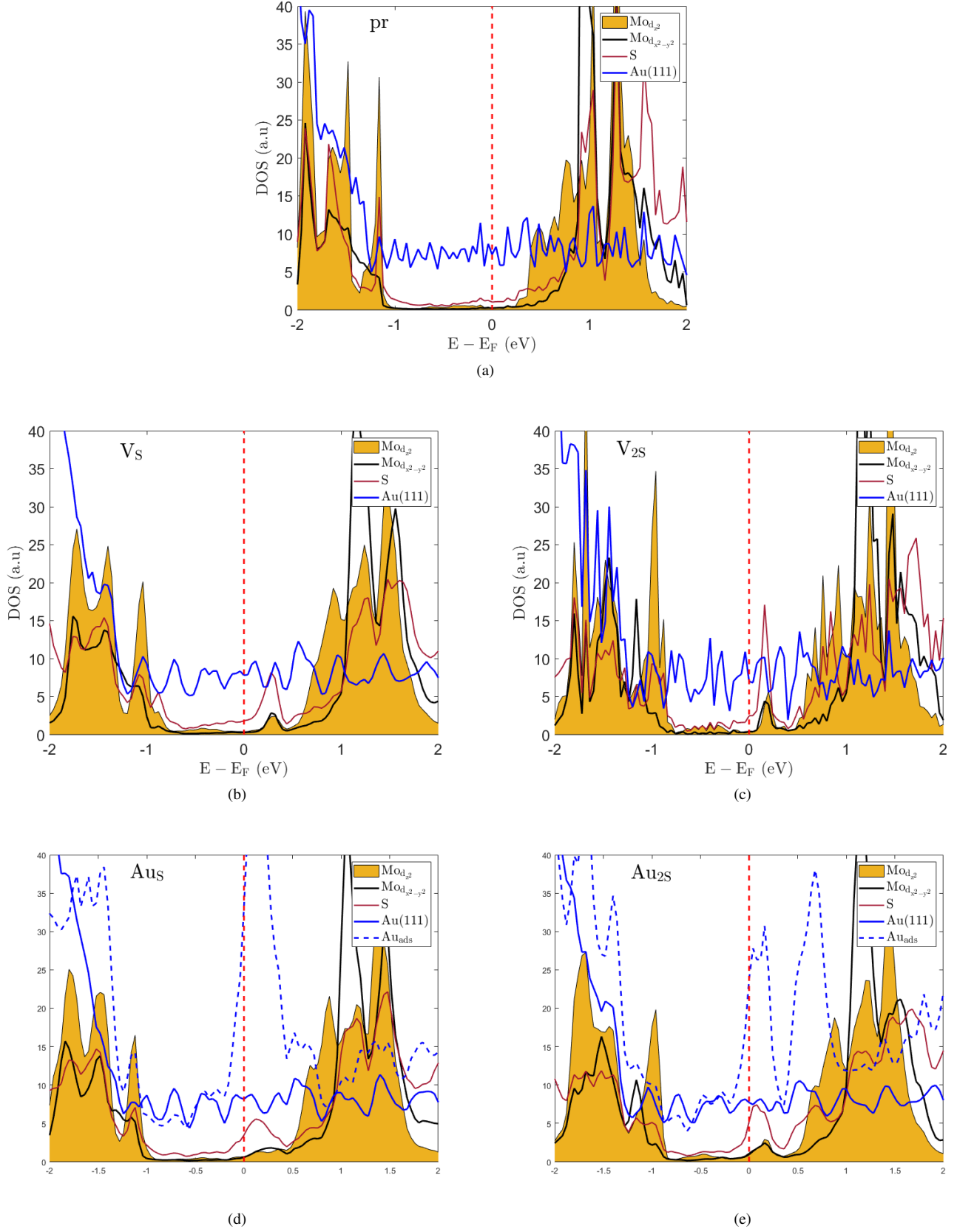


FIG. S16. PDOS of defect complexes in MoS₂/Au(111) heterostructure under 1.24% biaxial strain. PDOS of Mo, S and Au_{ads} are multiplied by 50, 50 and 100, respectively for ease of eye.

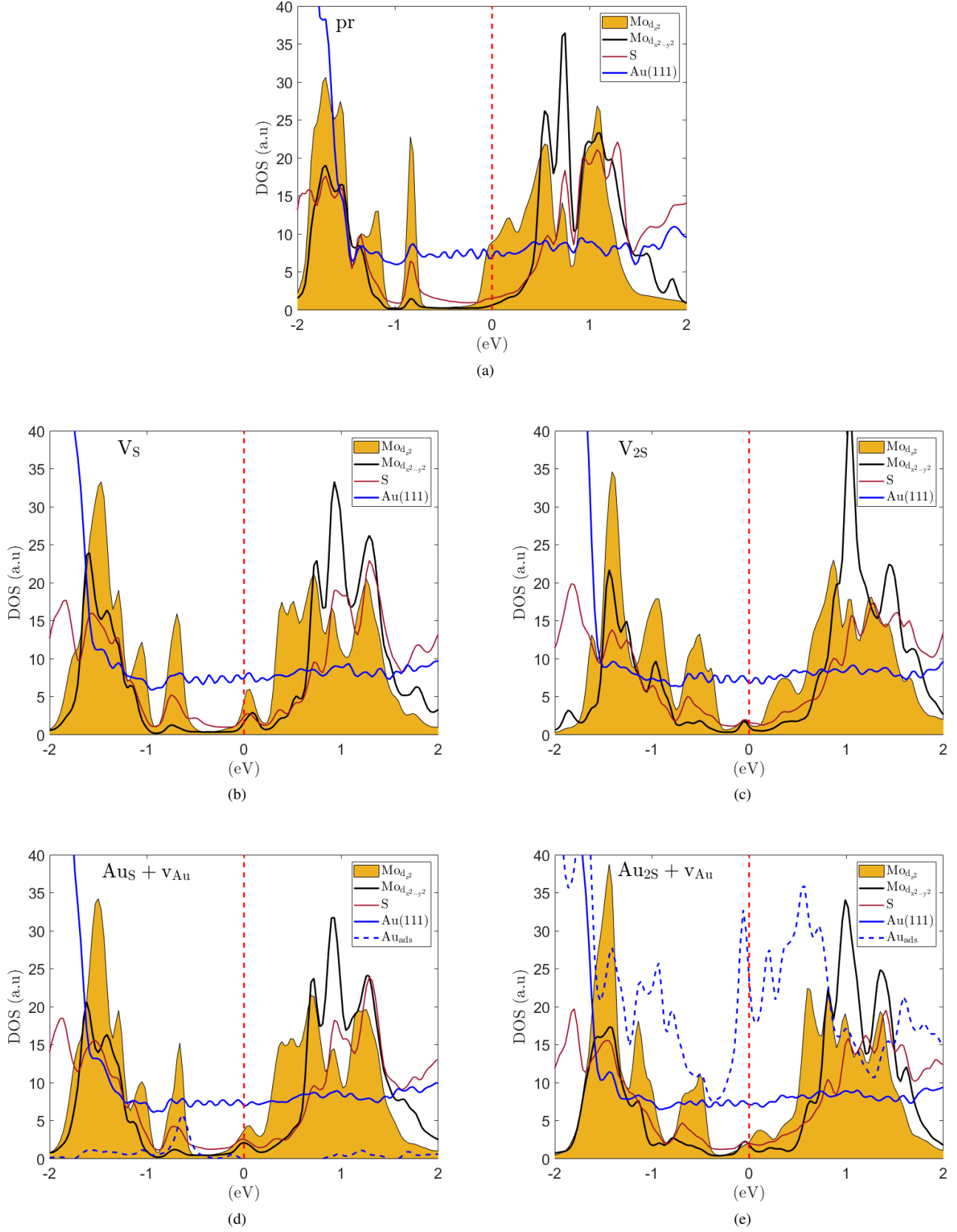
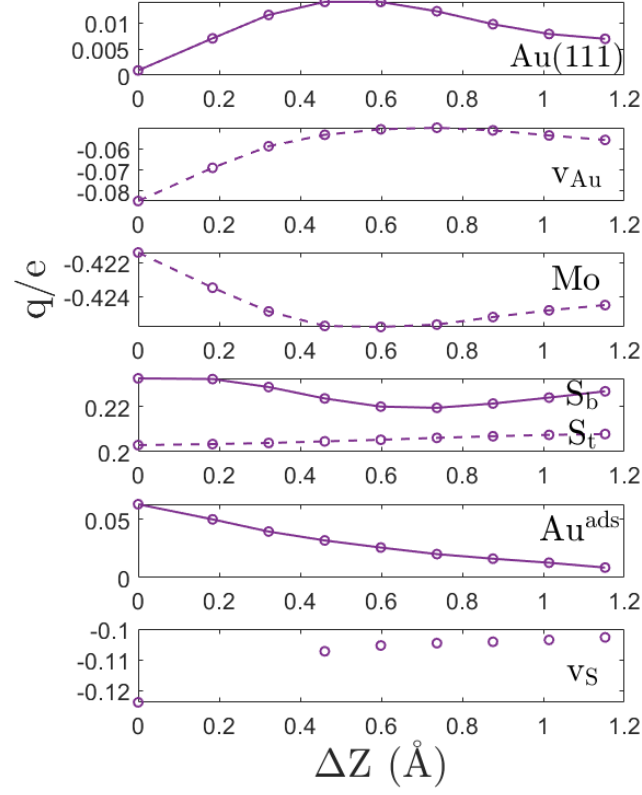


FIG. S17. PDOS of defect complexes in MoS₂/Au(111) heterostructure under 6.23 % biaxial strain. PDOS of Mo, S and Au_{ads} are multiplied by 50, 50 and 100, respectively for ease of eye.



(a)

FIG. S18. Changes of the Mulliken charge of atoms with interlayer distance in the $MoS_2/Au(111)$ heterostructure under 6.23% tensile strain.